June, 2019

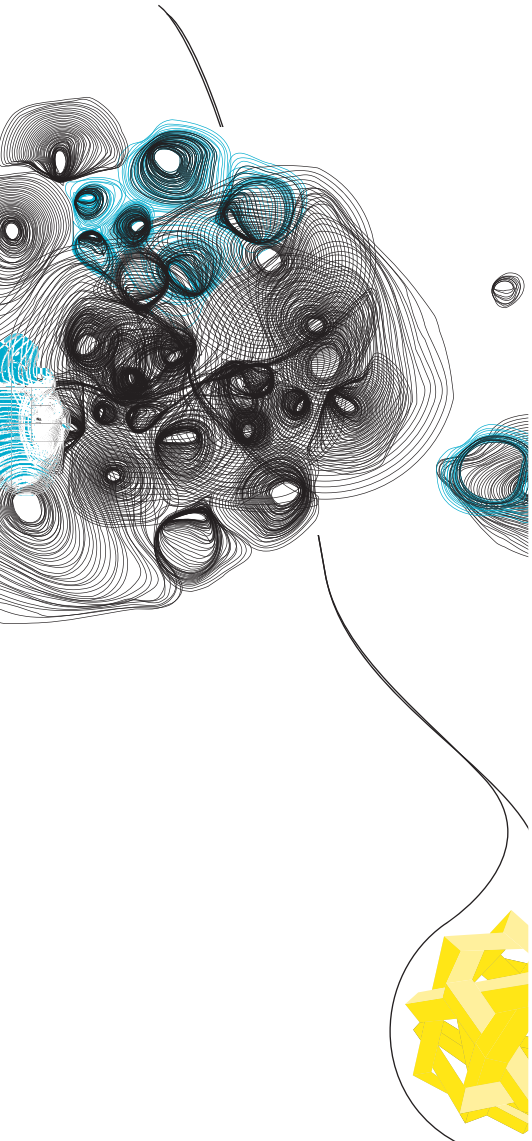

High-Frame-Rate Contrast-Enhanced Ultrasound Particle Image Velocimetry in the Stented Superficial Femoral Artery

A feasibility study

Master Thesis Technical Medicine
M. van Helvert

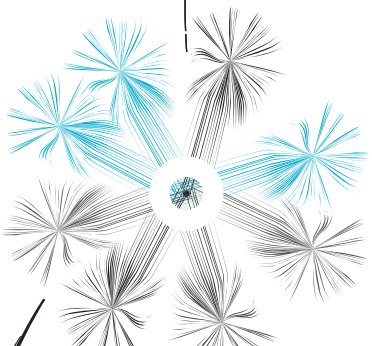

UNIVERSITY OF TWENTE.

Rijnstate

High-Frame-Rate Contrast-Enhanced Ultrasound Particle Image Velocimetry in the Stented Superficial Femoral Artery

A feasibility study

Author

M. van Helvert
Graduate student Technical Medicine
Medical sensing and stimulation track
Clinical specialization internship at Rijnstate hospital Arnhem
Department of vascular surgery

Graduation committee

Chair & technical supervisor	Prof. dr. M. Versluis
Medical supervisor	Prof. dr. M.M.P.J. Reijnen
Technical & daily supervisor	Dr. E. Groot Jebbink
Process supervisor	Drs. R.J. Haarman
External member	Dr. E. Mos-Oppersma

Colloquium

Date	July 4, 2019
Time	10 AM
Place	Carré (CR) 3.022, University of Twente

Abstract

Purpose - Analysis of local blood flow patterns near stenotic lesions in the femoral trajectory may provide insight in progression of disease and improve its diagnosis and treatment. High-frame-rate contrast-enhanced ultrasound, or echo PIV, seems a promising technique in visualizing and quantifying local flow profiles. This thesis discusses the work that has been done in investigating the behavior of contrast agents used during echo PIV measurements (1) and presents the first assessment of clinical feasibility of echo PIV in patients recently treated with a stent in the superficial femoral artery (SFA) (2).

Method - (1) Microbubble behavior was investigated experimentally in a controlled flow set-up. US data were captured with increasing transmit voltage and number of pulse cycles during three different steady flow conditions. Data were analyzed in the frequency domain before and after manually applying pulse inversion (PI).
(2) Clinical echo PIV measurements were performed at five different locations near the femoral bifurcation and the stented SFA in a pilot of twenty patients. Vessel visibility and contrast-to-background ratio (CBR) were evaluated as a measure of image quality. Accuracy of PIV was analyzed using the maximum normalized cross-correlation value and peak systolic velocity compared to duplex US.

Results - (1) Bubbles were visible in all measurements after PI was performed. In general, the intensity of the fundamental frequency was more present in the received signal from the microbubbles relative to the second harmonic frequency. Intensity of the fundamental frequency increased with increasing flow.
(2) Echo PIV data of twelve patients was successfully acquired. Quality of the measurements showed varying results in terms of vessel visibility and CBR between and within patients. Data of one patient was further analyzed through PIV. In two out of five locations adequate PIV results were found, showing high cross-correlation values and a velocity difference within 10% compared to duplex US.

Conclusion - (1) Bubble visualization was accomplished based on decorrelation between the two acquisitions needed for PI due to motion of the microbubbles causing imperfect cancellation of the fundamental frequency. Methods to better utilize non-linear behavior of the contrast should be further investigated.
(2) First assessment of echo PIV showed varying results which seem linked to the quality of the obtained data. Accurate blood flow velocity tracking was established in data with high CBR values. More data should be analyzed and improvements in PIV methods should be explored in order to draw a thorough conclusion regarding feasibility of echo PIV in quantifying blood flow in the femoral bifurcation and the stented SFA.

Preface

The work that lies before you is the product of my final year as technical medicine student. Twelve months ago I started my graduation internship at the department of vascular surgery of the Rijnstate hospital, a place where I happily returned after conducting a short internship during my second year of the technical medicine master's program. During this final year I found myself performing rather technical measurements in a very clinical setting. The responsibility of a clinical study gave me the opportunity to develop myself as a clinician. The technical aspects, on the other hand, gave me numerous input to let the engineer in me come to the surface. In my eyes the perfect combination.

This final year has brought me a lot. I would like to acknowledge the people involved. First of all I owe a great deal of thanks to all my supervisors. The very first day we started off with an M&M meeting in which I felt welcome right away, not only because of the first letter of my name but also due to the pleasant atmosphere. Michel, thank you for the continuous encouragements and optimism in both clinical and academical setting. The freedom and trust that you gave me throughout this year, for instance during outpatient clinical consults, has really helped building my self-confidence and brought me back to what I always wanted; developing myself as a more clinically oriented technical physician. Erik, thank you for always having the time to answer my questions and to discuss new ideas. Your help in the lab during my in vitro experiments was very much appreciated. Michel, your expertise on microbubbles and ultrasound has kept me fascinated. Your technical guidance and detailed questions during our meetings always gave me new ideas and broadened my knowledge. Rian, thank you for your guidance during the past two years. You were always there to listen and help me reflect. The moments of intervision have really grown on me. I recognize a lot of situations in my daily life in which I can apply the lessons learned. Guillaume, you helped me through multiple setbacks during the in vitro experiments. Thank you for your assistance and optimism. You once said; if it is easy, we wouldn't do it. I will keep this in mind. Stefan, you have contributed in numerous areas during the past year. First of all, thank you for your supervision of the clinical trial. I appreciate all the moments you were available to answer questions and discuss outcomes of measurements or new ideas. Moreover, thank you for proofreading this thesis. Your feedback is both useful and hilarious at the same time, it kept me going.

I would like to acknowledge everyone who helped during the echo PIV measurements. First of all, Marije, thank you for the hard work you have done in establishing this clinical trial. Everything was set perfectly, which resulted in a smooth transfer between us and a good further course of the trial. The vascular sonographers: Pinel, Laura, Frans, Bastiaan and Jochem, thank you for your enthusiasm and curiosity during the measurements. Your

assistance really helped to obtain the best possible echo PIV data. In this context I would also like to thank the people involved in the echo PIV meetings at the Erasmus MC. With your technical expertise we were able to optimize our measurements and perform the very first PIV analysis. Jason, thank you for sharing your knowledge and work on PIV.

Finally, I would like to thank my family. Mom, dad and my brother thank you so much for always being there for me. Even though you did not always understand what I was doing, I could share every single thing that was on my mind. You have helped me in staying optimistic and seeing the light at the end of the tunnel through your endless belief in my abilities. I am very grateful to have you as my family.

Majorie
June, 2019

Contents

List of Abbreviations

ABI	Ankle-brachial index
BMF	Blood mimicking fluid
CBR	Contrast-to-background ratio
CEUS	Contrast enhanced ultrasound
CFA	Common femoral artery
CFD	Computational fluid dynamics
CT	Computed tomography
DUS	Duplex ultrasound
FFT	Fast Fourier transform
HFR	High frame rate
MI	Mechanical index
MLA	Multiline acquisition
MRA	Magnetic resonance angiography
MRI	Magnetic resonance imaging
PAD	Peripheral arterial disease
PFA	Profunda femoral artery
PI	Pulse inversion
PIV	Particle image velocimetry
PSD	Power spectral density
PSV	Peak systolic velocity
PTA	Percutaneous transluminal angiography
PVA	Polyvinyl alcohol
PW	Plane wave
RF	Radio frequency
SFA	Superficial femoral artery
SNR	Signal-to-noise ratio
SVD	Singular value decomposition
UCA	Ultrasound contrast agent
US	Ultrasound
WSS	Wall shear stress
WT%	Weight percent

0 Introduction

Peripheral artery disease (PAD) of the lower extremities is a serious health issue for the elderly in the modern era. The Dutch heart association predicted a 46% relative increase in prevalence of PAD amongst the Dutch population between 2011 and 2040. [1] Patients often present themselves with symptoms of severe muscle pain, induced by walking and relieved by standing still. Progression of disease could cause critical ischemia, leading to pain at rest or necrosis. [2] These symptoms adversely effect quality of life and functional status. [3] Moreover, PAD patients, both with and without symptoms, have an increased risk of cardiovascular events. [4] The underlying pathology of this increased risk is the systemic disease process atherosclerosis.

Atherosclerotic plaques impede adequate blood supply to targeted tissues. Systemic atherogenic risk factors have been well identified. The influence of the local arterial microenvironment has only recently been addressed more extensively. [5] The formation of plaques tends to localize at specific arterial regions of curvature and branch points. In these regions, the endothelial cells are exposed to nonuniform flow and irregular distributed low shear stresses. Low shear stresses are generally correlated to upregulation of proatherogenic genes and proteins by the endothelial cells. [6] Visualization of blood flow on a local scale could help understand the role of complex flow patterns on the pathogenesis of vascular diseases. Hence, successful blood flow quantification provides an important step towards being able to predict atherosclerotic disease progression.

Current treatment guidelines for the femoro-popliteal trajectory indicate endovascular revascularisation in all lesions with a total length up to 25 cm. [7] Despite continuous advancements in the field of endovascular revascularisation, in-stent restenosis remains a difficulty in the treatment of lesions in the femoral arteries. [8, 9] Here too, locally disturbed blood flow may play a major role. The influence of stent placement on blood flow patterns remains unknown. Visualizing and quantifying blood flow may advance endovascular treatment on a patient specific level.

High-frame-rate contrast-enhanced ultrasound particle image velocimetry (echo PIV) is a recent development in the field of human blood flow quantification. Echo PIV has proven its feasibility in the abdominal aorta and carotid artery in a pilot of healthy volunteers. [10, 11] Application of echo PIV in a population of PAD patients with femoral occlusive disease, treated with a stent placement, has not been reported yet. The evaluation of its potential for clinical applicability in the field of vascular surgery is an ongoing process in our group.

This thesis is the product of a year of work on conducting a clinical feasibility study investigating echo PIV in the stented femoral artery. The outline of this thesis is as follows. The first chapter introduces all aspects of femoral artery occlusive disease. Moreover, the relation between local blood flow patterns and its pathogenesis is discussed. The second

chapter starts with an introduction of conventional ultrasound and its significant drawbacks in quantifying blood flow. Echo PIV is discussed in relation to these limitations and how they are overcome. The third chapter elaborates on an in vitro experiment carried out to obtain more insight into the behavior of ultrasound contrast agents. These experiments originated from previous observations during echo PIV measurements in the clinical setting. Clinical feasibility of echo PIV is discussed in the fourth chapter. A method to assess feasibility is described and an overview of the first results of the clinical trial are given. Finally, this thesis is concluded with a general conclusion on the most important findings given in the fifth chapter.

1 Femoral artery occlusive disease

As a result of an aging population, cardiovascular disease has become a major health issue. Peripheral arterial disease, or PAD, is most commonly caused by atherosclerosis. This systemic disease process causes obstruction of the vessel lumen, compromising blood flow to targeted tissues in the lower extremities. Over 200 million people worldwide have PAD, with or without symptoms. [12] Symptomatic PAD occurs often due to stenosis or occlusion of the femoropopliteal trajectory. Roughly 70% of the lesions are located in this area. [13, 14] Systemic risk factors for PAD are well identified and similar to risk factors of other atherosclerotic vascular diseases. These risk factors include diabetes mellitus, hypertension, hyperlipidemia, age and lifestyle (e.g. cigarette smoking and physical inactivity).

1.1 Pathogenesis

Atherosclerosis is a multifactorial systemic and chronic disease of the arterial wall. Initial steps of the disease process include activation of the endothelial cells, which form the intimal layer of the arterial wall. Activation induces the expression of specific adhesion molecules on the surface of these cells. These adhesion molecules are involved in recruiting leukocytes to the intimal layer. Captured leukocytes migrate into the intimal layer and mature into macrophages. The macrophages accumulate lipids evolving into a fatty streak, roughly seen as the earliest recognizable stage of atherogensis. This inflammatory response of the intimal layer activates smooth muscle cells in the medial layer. Activated smooth muscle cells change their phenotype, migrate and accumulate into the lesion. They deposit an extracellular matrix, causing the plaque to become more fibrous. A necrotic core may occur due to the accumulation of cellular debris. More advanced plaques also contain cholesterol crystals and microvessels. [15, 16, 17]
Plaque formation tends to localize at specific locations in the arterial vascular bed as presented in Figure 1.1A. [5] These are typically locations of curvature and branch points, experiencing disturbed blood flow dynamics. [18] local blood flow seems to play a localizing role in atherosclerotic plaque formation. In straight vessels, a parabolic flow profile, e.g. laminar flow, is assumed. This pattern is the result of friction between fluid layers and friction between the fluid and the vessel wall. The latter creates a tangential force exerted on the arterial wall, referred to as wall shear stress (WSS). WSS is defined as:

$$\tau_w = \mu \frac{\delta v}{\delta r}, \tag{1.1}$$

with μ presenting the viscosity of blood, v the velocity of blood along the vessel axis and r the inward distance perpendicular to the wall. [19] Locations exposed to low or oscilla-

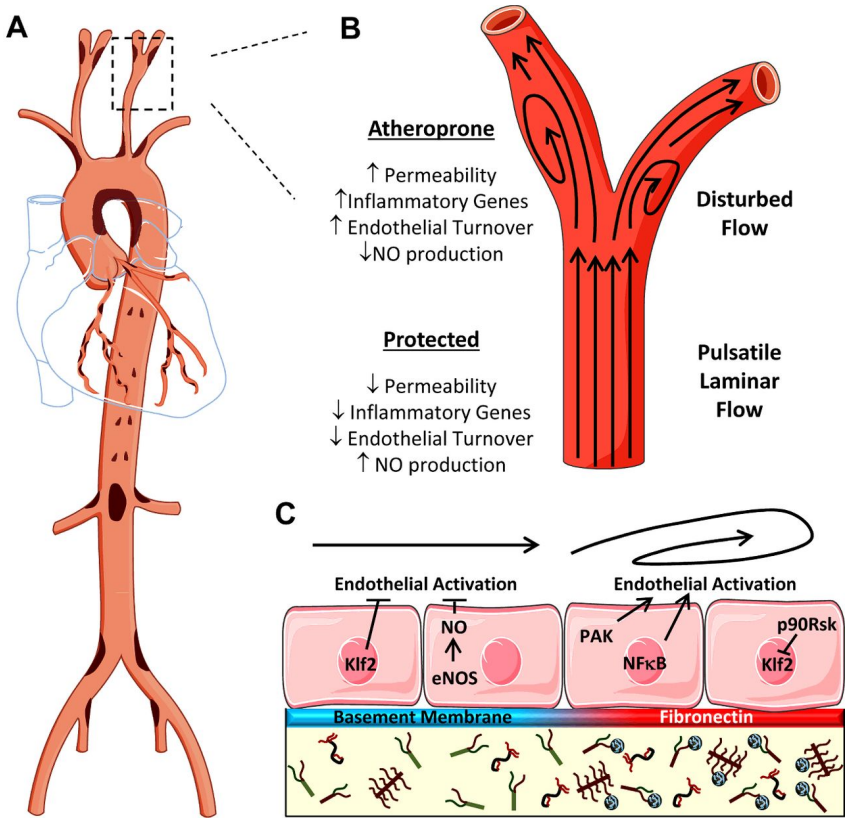

Figure 1.1: *Arterial blood flow and atherosclerosis.* ***(A)*** *Plaque formation throughout the arterial tree with preferred locations colored in brown.* ***(B)*** *Relation between different blood flow profiles and atheroprone or protected changes of the endothelial cell phenotype.* ***(C)*** *Endothelial activation mechanisms and corresponding extracellular matrix composition related to blood flow changes. Reproduced from Yurdagul et al. [5]*

tory fluid shear stress, such as the outer walls of a bifurcation, are related to plaque formation. This phenomenon and corresponding mechanisms are illustrated in Figures 1.1B and C. [5] Endothelial cells exposed to higher WSS tend to elongate and align in a clear organized pattern, whereas cells experiencing low WSS have no preferred pattern. Moreover, low wall shear stresses alter the endothelial cell gene and protein expression towards a pro-atherogenic phenotype. Hence, this specific fluid-mechanical stimuli influences the onset and progression of plaque formation. [5, 19, 20, 21]

1.2 Clinical manifestations

Symptoms of PAD vary between patients, depending on the location and size of the lesion, metabolic demands of the ischaemic tissue and the presence or absence of collateral circulations. [22] Clinical presentation of a patient is commonly scored using the Fontaine classification, in the Netherlands, or the Rutherford classification in other countries. Both

are presented in Table 1.1. The first clinical and most common sign of PAD is intermittent claudication. Intermittent claudication is characterized by fatigue, discomfort or severe pain of the muscles distal to the lesion during exercise, and relief of this pain at rest (Fontaine II). In case of stenosis or occlusion of the superficial femoral artery (SFA) this pain is mostly present in the calf. Other early signs of PAD include diminished or absent pulses of the femoral-, dorsalis pedis- and/or posterior tibial artery, arterial bruits, pallor on elevation and decreased capillary refill. When PAD progresses patients may experience pain at rest (Fontaine III) non-healing wounds or gangrene (Fontaine IV), as a consequence of insufficient blood supply. [23, 24]

The first step in diagnosing PAD, after clinical examination, is to measure the ankle-brachial index (ABI). The ABI is calculated as the ratio between systolic blood pressure at the ankle (measured at the posterior tibial- or dorsalis pedis artery) and the right or left brachial artery. All pressures are obtained in supine position using an ultrasound probe with continuous-wave Doppler to trace the Doppler signal and an inflatable cuff around the calf and upper arm attached to a sphygmomanometer to measure the systolic pressure. An ABI $\leq$0.9 indicates the presence of PAD. [22, 23, 26] Values between 0.91-0.99, or >0.99 with clinical suspicion of PAD need further diagnostics. [24] Additional diagnostic tests include duplex ultrasound (US), contrast enhanced CT or MRA-scanning. Invasive angiography may be used in more complex cases. Duplex US is considered as the first-line imaging method incorporating 2-dimensional gray-scale US to provide visualization of the lesion and pulse-wave Doppler to determine flow velocities. The influence of the stenosis on hemodynamics can be assessed directly by measuring the changes in peak systolic velocity (PSV) proximal and distal to the lesion. [23, 27] Approximately, a doubling of the PSV ratio (1.8-3.0), indicates a stenosis >50%. The PSV ratio is, however, not accurate enough to evaluate the hemodynamic significance of the stenosis. [27]

When revascularization is considered, a second imaging technique is usually required. Both contrast enhanced CT and MRA give reliable information regarding the anatomy of the lesion. CT can visualize calcifications more accurately, which is useful to estimate the severity of the stenosis. Based upon the scan results, a patient specific treatment can be initiated. [24]

Table 1.1: *Classifications of peripheral arterial disease of the lower extremities; Rutherford and Fontaine classification. [25]*

Rutherford Classification			Fontaine Classification	
Grade	Category	Description	Stage	Description
0	0	Asymptomatic	I	Asymptomatic
I	1	Mild claudication	IIa	Mild claudication
I	2	Moderate claudication	IIb	Moderate to severe claudication
I	3	Severe claudication		
II	4	Ischemic rest pain	III	Ischemic rest pain
III	5	Minor tissue loss	IV	Ulceration or gangrene
III	6	Major tissue loss		

1.3 Treatment

Patients diagnosed with PAD will receive treatment with the aim to address the risk factors important in the progression of systemic atherosclerosis, to preserve limb viability and to improve functional capacity. PAD patients are associated with a higher risk of adverse cardiovascular events, hence secondary risk prevention is necessary. Secondary risk prevention focuses on smoking cessation, accurate nutrition, antiplatelet therapy and treatment of other risk factors such as hyperlipidemia, hypertension and diabetes [2, 16, 26, 28] This risk factor modification can greatly reduce progression of PAD. [26]

To improve the functional capacity, supervised exercise therapy is indicated. Regular supervised exercise improves the maximum and pain free walking distance and quality of life. The most important mechanism behind these improvements is the progression in collateral circulation, redirecting the blood to the tissue. [2, 22] In a random controlled trial, supervised exercise resulted in a significantly higher mean peak walking time after 6 months compared to primary stenting. [29]

When sufficient progress in functional capacity is not achieved, and symptoms severely compromise daily life activity, revascularization is considered. Revascularization is also indicated in case of critical limb ischaemia, expressed as pain at rest or tissue loss secondary to PAD (Fontaine III and IV), to prevent limb loss. Without revascularization, 23% of the limbs presented with ischaemic ulceration treated with wound-healing techniques only, require amputation within 1 year. [30]

Different revascularization methods co-exist; open surgical and endovascular strategies. For the femoral trajectory, surgical endarterectomy is used to treat plaques located in the common femoral artery (CFA) or at the bifurcation. Although it was recently shown that stent placement can be effective here too. [31, 32] In case of the superficial femoral artery (SFA), surgical approaches, e.g. femoropopliteal by-pass surgery with a synthetic or autologous graft, have been the principal method for a long time as well. [7] However, due to improvements in the field of endovascular revascularization, these methods are increasingly applied as primary treatment of stenotic lesions in the SFA. [33, 34] There is a lack of evidence to demonstrate the superiority of one method above the other. [35] The latest ESVS guidelines suggest endovascular revascularization as main approach for all lesions up to a total length of 25 cm. [24] Most important, besides the anatomic complexity of the lesion, patients' comorbidity, predicted response to treatment, overall prognosis, experience of the center and availability of autologous conduit have to be considered while assessing both methods. [7]

1.4 Endovascular revascularization

Percutaneous transluminal angioplasty (PTA) has a less invasive character and has been recognized as an efficient and safe method to treat short femoropopliteal lesions. [34] However, the SFA is prone to restenosis after PTA. Primary patency rates for treated lesions <10 cm ranges between 65-77% at 1 year and 42-55% at 5 years. [36] Restenosis occurs due to intrinsic biomechanic and hemodynamic properties of the SFA and its surrounding muscles. The interaction between material used during PTA and the intimal

layer of the vessel may trigger an inflammatory response. This response leads to intimal hyperplasia, which also contributes to restenosis. [9, 37, 38]
Stent placement is considered to improve these patency rates. Results of different clinical trials imply that PTA alone is sufficient in short lesions (<10 cm) and PTA with stenting is recommended in intermediate length of lesions (between 10-15 cm). [8, 38] Over the years, multiple iterations of stents with different features have been introduced and used in clinical practice. The first generation consisted of balloon expandable stents, followed by self-expanding nitinol stents with thermal memory. The nitinol stent showed better flexibility, is more fracture-resistant and is, nowadays, the most commonly placed stent in patients with a femoropopliteal lesion. [9, 38] However, these stents still show fracture rates of 20% at 18 months and in-stent restenosis rates of 21.1% at 24 months. [39] Thus, stent fractures and in-stent restenosis remain a considerable problem. Risk factors of in-stent restenosis include positioning, length, diameter and oversizing of the stent. Furthermore, the interaction between stent material and vessel wall and a poor distal runoff score are reported. [9, 40] A third generation of superflexible nitinol stents with modified stent-cell interconnection structures has been designed and shows promising short-term (6 months follow-up) outcomes. [37] To prevent intimal hyperplasia and reduce (in-stent) restenosis, drug-eluting balloons and stents were introduced. Another stent design to decrease intimal hyperplasia is the covered stent, consisting of a polytetrafluoroethylene liner attached to a nitinol stent structure.
The past decade, numerous clinical trials have been performed to test and compare primary and secondary patency, restenosis rates and clinical outcomes of the different stent types. There is a discrepancy in outcomes, mainly due to difference in lesion types and lengths. Yiu et al. [8] and Marmagkiolis et al. [38] conclude a high variety of effective endovascular treatment modalities and predict a further trend towards endovascular revascularization.
In longer and more complex lesions an open surgical bypass is still considered as the golden standard. However, due to continuous advancements of endovascular treatment modalities, such as long stent-graft segments up to 25 cm of the covered stent and an improved proximal edge design, it is gaining acceptance as primary treatment of more complex lesions as well. A clinical trial comparing the covered endoprosthesis to an open surgical bypass showed no significant differences in long-term outcomes (4 years) of primary and secondary patency rates. [41] 1-year results of another study comparing both approaches showed that the covered stent is related to faster recovery, less morbidity and faster improvement of quality of life and the patency rates were, again, similar. [42]

2 Contrast enhanced ultrasound particle image velocimetry

Local blood flow influences the process of plaque formation and stent patency in terms of restenosis. This relation emphasizes the importance to investigate local blood flow characteristics near stenotic lesions. Quantifying flow properties can be done with different in vitro en in vivo methods. Computational fluid dynamics (CFD) can be used for numerical analysis and data structures to solve fluid flow problems. In vitro methods consist of phantom models and flow circuits to imitate vessel geometries and physiological (pulsatile) blood flow. Applicability of in vitro measurements and outcomes for clinical set-ups will, however, always be limited by the deviation between in vitro and in vivo environments. [43] Magnetic resonance imaging (MRI) is a promising technique to obtain in vivo flow components. However, MRI is time-consuming, requires breath-holds, has a poor temporal resolution and does not always work accurately near stents. US Doppler is, nowadays, often used in clinical practice to obtain local velocity measures. Although US is an effective, low-cost and easy to use technique it is limited by the angle dependence, low frame-rate acquisition and poor accuracy near the blood-wall interface. Moreover, conventional US cannot determine the 2D vector field with high resolution across the vessel diameter. [43, 44]

2.1 Medical ultrasound

US imaging principles are based on the differences in acoustic impedance between different types of tissue, i.e. differences in density or compressibility of the tissue. An US pressure wave gets generated and transmitted with a certain central frequency by the piezoelectric elements of the transducer. The US wave propagates through the tissue and gets attenuated, i.e. loses energy, as it travels further. Attenuation of the US wave mainly occurs due to absorption and scattering. Absorption is the conversion of motion energy to thermal energy by the insonified tissue. Scattering is defined as a deviation of a part of the US signal from its original direction. Scattering occurs at the interface between tissue structures with a difference in acoustic impedance. The size and shape of the scatter object compared to the incident wavelength influences the way of scattering. In medical images diffuse scattering is most prominent. The scattered signal partly travels back to the transducer, i.e. backscatter, and yields essential information regarding the amplitude, phase and frequency required to obtain US images and blood velocity estimates. The distance of the scatter object can be derived from the travel time of the US wave, as there is little variation in speed of sound in human tissue [45, 46]
In medical US different transducers are used. The most common types of transducers are the (curved) linear and phased array probes. Each transducer has a different amount of piezoelectric elements and a specific frequency bandwidth in which it emits and receives

ultrasound. Frequencies used in medical ultrasound range between 1-20 MHz. Based on the desired depth and image quality a certain central frequency is preferred. Higher frequencies (10-15 MHz) attenuate faster and are therefore used to visualize superficial structures. Conversely, lower frequencies (2-5 MHz) penetrate deeper into tissue. [47]

Image quality

When generating an image with conventional US, a section of the elements, the aperture, is activated and emits an US pulse. As soon as the reflected pulse is received back at the transducer, the next section of elements will emit an identical pulse. The number of pulses emitted in one second is referred to as the pulse repetition frequency. The duration of a pulse depends on the number of cycles in the pulse and the period of one cycle (inversely related to the transmitted frequency). Each pulse and its reflected signal will contribute to one scan line and all scan lines together construct the complete image. The time it takes to obtain one image influences the frame rate, i.e. the temporal resolution. A sufficient temporal resolution is essential in determining velocities.
There is a trade-off between temporal- and spatial resolution. In conventional US each emitted beam is focused to obtain the optimal spatial resolution. Spatial resolution is divided in axial and lateral resolution. Axial resolution is the minimum distance at which two points in the axial direction of the beam can be distinguished. A shorter spatial pulse length, caused by either less cycles per pulse or a higher frequency and consequently shorter wavelength, increases the axial resolution.
Current transducers are designed with as little cycles per pulse as possible. Lateral resolution is described as the minimum distance between two separated points perpendicular to the beam. Lateral resolution depends on the width of the beam. Decreasing the width of the beam, i.e. creating a focus, will improve lateral resolution. However, this limits the field-of-view. [45, 46, 48]

Velocity estimations

In current clinical practice, blood flow velocity estimates are based on the Doppler effect. This phenomenon specifies the frequency shift caused by a moving source, in this case an erythrocyte, relative to the fixed transducer. If the erythrocyte moves towards the transducer its echo consists of a higher frequency than the transmitted frequency. Vice versa, when the erythrocyte moves away from the transducer the frequency decreases. The difference between the incident frequency and the received reflected frequency is called the Doppler frequency, or Doppler shift, (f_d). The relation between f_d and the velocity is as follows:

$$f_d = 2f_0 \frac{v cos(\theta)}{c}, \tag{2.1}$$

in which f_0 represents the incident frequency, c the speed of sound in tissue, v the velocity of the blood at angle θ with the transmitted US signal. Velocity estimates based on this equation are performed using continuous-wave and pulsed-wave US signals. Pulsed-wave US has the advantage that it can discriminate the depth at which the echo originated from. [45] From the $cos(\theta)$ term an important drawback of this method becomes clear; the

angle-dependency. Only projections of velocity parallel to the US signal can be measured accurately. Other limitations are the assumptions that blood flow is unidirectional, that the vessel walls are uniformly straight and that flow is steady, laminar (aligned with the vessel wall) and non-oscillatory. The minimum and maximum detectable velocities are both limited by the selected pulse repetition frequency. [45, 49]

2.2 Echo PIV

To overcome the angle dependence and obtain a more accurate velocity estimation, particle image velocimetry (PIV) has been introduced. Principles of PIV analysis are based on tracking small groups of particles in subregions, i.e. interrogation windows, of the captured image. The mean displacement of the particles in one window is calculated using a cross-correlation algorithm between the same interrogation windows in two successive images. For each possible displacement the cross-correlation is determined and the highest peak of the correlation matrix gives the most probable displacement. This computation is performed in the frequency domain after fast Fourier transform (FFT). The different steps of PIV analysis are illustrated in Figure 2.1. [50] The size of the interrogation window influences the spatial resolution of PIV and the dynamic range in velocity. Smaller window size increases the spatial resolution, but decreases the signal-to-noise ratio (SNR) of the correlation peak and the dynamic range in velocity due to loss of matching particles. Therefore the size of a sub region is based on the maximum permitted displacement of the particles, which should not exceed $\frac{1}{4}$ of the window (one-quarter rule). To improve spatial resolution, SNR of the correlation peak and the dynamic velocity range, multiple passes of the FFT can be performed on the same data-set. The first cross-correlation analysis is used to offset the interrogation window in the following passes. The next interrogation window may be deformed (to increase accuracy), reduced in size (to increase spatial vector-resolution) and/or moved in the direction of displacement. Finally, flow dynamic parameters can be derived from the achieved vector velocity maps. [11, 44, 51, 52]
Echo PIV is an easy-to-use technique with good repeatability and reproducibility. [49] In vitro it has been validated by directly comparing flow velocity profiles of continuous and pulsatile flow environments with analytical solutions and/or optical PIV, which is the golden standard. [43, 44, 51, 53, 54]. All studies found sufficient agreement with the reference data, well within 10%. Using careful analysis methods and well-defined and controlled measurement conditions, the random error in velocity estimates can be limited to 1%. Hence, in principle echo PIV has a comparable accuracy to optical PIV. [55, 56] Conventional optical PIV cannot be used in vivo because it requires optical access. [51] In vivo comparison of echo PIV and phase enhanced MRI measurements of the carotid artery in healthy subjects showed a good agreement with a correlation of 0.89. Quantitatively however, a significant difference in WSS values was found. [49, 54] Furthermore, feasibility of echo PIV to measure flow patterns in the abdominal aorta in healthy volunteers has been proven. [10]
The dynamic velocity range that echo PIV measurements can obtain depends on the available frame rate. Higher frame rates result in a better temporal resolution and the possibility to measure higher velocities. However, in conventional B-mode scanning, it comes

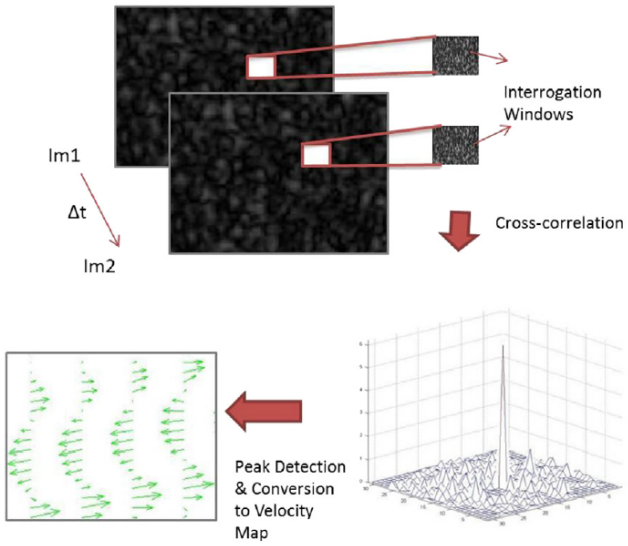

Figure 2.1: *Principle of conventional particle image velocimetry. First two successive images are divided into small interrogation windows. Second, the cross-correlation between the successive interrogation windows is calculated and the peak of the cross-correlation map displays the most probable displacement of the particles. The location of the peak is detected and converted to one velocity vector. Ultimately, this is done for each interrogation window, resulting in a velocity vector map. Reproduced from Leow et al. [50]*

at the cost of the field-of-view. [49] To overcome this limitation different advanced US techniques resulting in high-frame-rate (HFR) acquisitions were introduced.

2.3 High frame-rate imaging

The most commonly known methods to increase frame rate include plane wave (PW) excitation and multiline acquisition/transmit systems. Multiline acquisition (MLA) techniques are implemented in the newest conventional US systems and construct multiple neighbouring scan lines from each transmitted beam. For instance, a 4MLA system constructs four scan lines simultaneously, increasing the frame rate 4-fold. MLA techniques may be combined with multiline transmit systems in which multiple focused beams are transmitted at the same time. Image quality of these systems is competitive with conventional captured images. [45, 48]

The physical maximum in frame rate is achieved when using PW. In PW, all elements of the transducer transmit and receive synchronously. By introducing a linear delay between elements, the planar wave-front gets tilted to obtain an angled acquisition. However, due to a lack of focusing and increased side lobes in the received signal, image quality decreases significantly. [57] To improve lateral resolution, coherent spatial compounding of multiple angled acquisitions can be performed. This way, images with comparable quality to conventional US are achieved. [45, 48] This effect is illustrated in Figure 2.2. By using

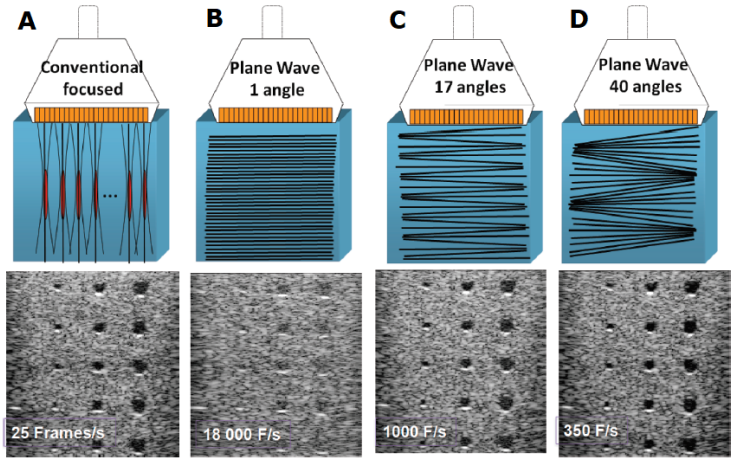

Figure 2.2: *The effect of plane wave (PW) imaging on frame rate and image quality.* ***(A)*** *Conventional focused imaging. 128 focused beams are used and lead to a frame rate of roughly 25 frames/s.* ***(B)*** *PW imaging using 1 angle. Frame rate increases till 18.000 frames/s. Corresponding image quality decreases.* ***(C-D)*** *PW compounding of multiple angles with improved image quality compared to 1 angle. Given frame rates correspond to a 4 cm deep region of interest. Reproduced from Tanter & Fink [58]*

this HFR technique, Leow and coworkers were able to track the evolution of flow during a complete cardiac cycle in vivo in the rabbit aorta. They managed to increase the frame rate 40-fold (using a three-angled compounding and pulse inversion sequence), which enabled the tracking of velocities up to 80-100 cm/s at an approximate depth of 10 mm. [50]

2.4 Microbubbles

To enhance the echogenicity of blood, microbubble-based ultrasound contrast agents can be used. Ultrasound contrast agents (UCA) have a large difference in acoustic impedance compared to its surroundings and exhibit resonance. As a consequence, they can enhance the scattered signal with 20-30 dB compared to only blood cells. These contrast agents are gas-filled bubbles encapsulated by an extremely thin shell consisting of lipid, albumin or other surfactants. Due to the use of low solubility gases and the stabilizing properties of the surrounding shell, the microbubbles last longer in the blood stream and are sufficiently stable for the transit through the cardiopulmonary circuit. Clearance of the microbubbles happens mostly by disruption and gas exchange in the lungs. Other required properties of an efficient UCA are low toxicity, easy introduction to the blood stream and a low stokes number, so that they follow the blood flow accurately. [59, 60]

The extremely thin shell provides the flexibility needed for their acoustic response. Their scattering behavior can be divided into three broad regimes, depending on the peak pressure of the transmitted signal. First, for very low peak pressures microbubbles will scatter approximately linear, comparable to tissue. Second, if the intensity of the emitted signal increases, microbubbles start to show non-linear characteristics. This non-linear behavior

is a consequence of the asymmetrical vibration of a bubble, illustrated in Figure 2.3. At positive pressure, a microbubble gets compressed and becomes stiffer, hence resisting to a further decrease of its radius. In the rarefaction phase, at negative pressure, the microbubble becomes less stiff and expands much more. The natural resonance frequency, at which the bubble will scatter US with a high efficiency, lies around 3 MHz for bubbles with an average diameter of 3 μm. The resonance frequency increases for stiffer shells and smaller bubbles. Third, when the intensity of the transmitted signal increases even more, bubble disruption will occur. During disruption, scattering levels from the contrast agents increase rapidly for a short amount of time. This is an irreversible process. [59, 60, 61] PW excitation approaches showed less bubble disruption at higher transmitted intensities than conventional US methods. [62]

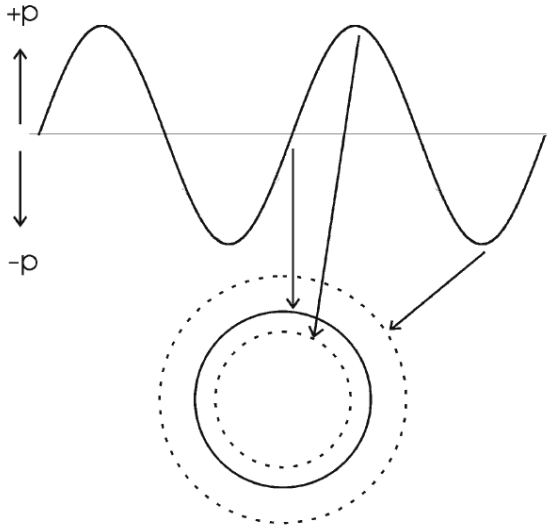

Figure 2.3: *Simplified model of the asymmetric vibration of a microbubble at different instances of the ultrasound pressure wave. Reproduced from E. Quaia. [60]*

2.5 Contrast harmonic imaging and pulse inversion

Several US imaging techniques make use of the specific non-linear properties of UCA. Due to non-linearity, the backscattered signal from the microbubbles contains higher harmonics of the fundamental transmitted frequency. Tissue scattering is considered to be mainly linear. Conventional contrast harmonic imaging uses this phenomenon to distinguish between tissue and UCA. This technique is based on the second harmonic frequency, as it contains the most power. Moreover, the frequency bandwidth of the transducer is too narrow to receive all higher harmonics accurately. [59, 60, 61] To obtain the second harmonic frequency, a high-pass or band-pass filter is applied to the received signal, removing all other frequencies. Harmonic contrast imaging requires a narrower transmit and receive bandwidth to avoid overlap in the fundamental and second harmonic frequency

bands. Hereby sensitivity to discriminate between tissue and UCA improves. Axial resolution, however, decreases due to the longer pulse length needed to narrow the frequency band. [59]
Pulse inversion (PI) techniques overcome this limitation and detect non-linear components of the backscattered signal over the entire bandwidth of the transducer. PI sums the received signal of two transmissions with opposite polarity, i.e. 180-degree phase change. Linear behavior is cancelled out, whereas non-linear behavior results in a detectable signal. This approach is illustrated in Figure 2.4 and will be discussed in detail in Chapter 3. [59, 60, 63] The effect of harmonic imaging and PI is demonstrated in Figure 2.5. [64]

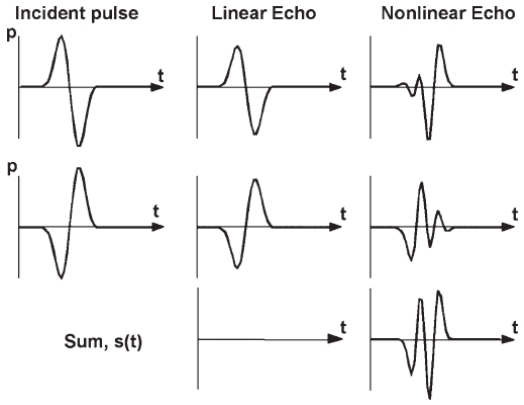

Figure 2.4: *The principle of pulse inversion imaging, based on the nonlinear behavior of the microbubble contrast agent. Two ultrasound pulses are transmitted, with 180-degree phase difference, into the tissue. The tissue behaves linear and the echoes will be inverted copies of each other. Summing them will cancel the signal to zero. The nonlinear echoes from the microbubbles are distorted inverted copies and will not cancel each other, resulting in a detectable signal. Reproduced from Wilson & Burns. [65]*

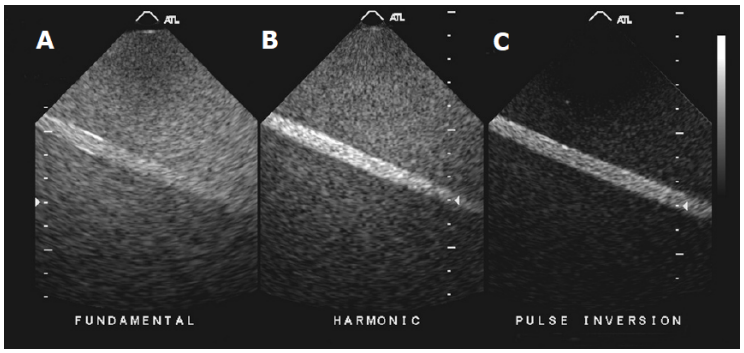

Figure 2.5: *The result of* ***(C)*** *pulse inversion compared to* ***(B)*** *harmonic imaging and* ***(A)*** *conventional fundamental imaging. A tissue mimicking phantom (biogel and graphite) was used together with Optison microbubbles to demonstrate the effect of different imaging techniques. Pulse inversion provides better contrast between tissue and microbubbles. Reproduced from Becher & Burns. [64]*

3 Bubble behavior - in vitro experiments

3.1 Introduction

Microbubbles are used as a contrast agent to enhance echogenicity of blood. The underlying properties of microbubbles, one of which is their non-linear response to insonation with increased acoustic power, are already discussed. [59, 60] It is this non-linear behavior which gives rise to new frequency components in the scattered signal. This phenomenon is the foundation of several contrast-specific ultrasound techniques, which proved to be more sensitive than fundamental imaging. Conventionally, the contrast harmonic signal is extracted from the received echo by filtering. This technique, however, has multiple limitations as described in Chapter 2. [63] These limitations are overcome by PI techniques in which the full bandwidth is used and non-linear UCA characteristics are enhanced by subtracting rather than filtering out the fundamental. A detailed explanation of PI is given in Chapter 2 and Figure 2.4. [66, 67] PI shows a higher sensitivity than second harmonic imaging due to better rejection of the fundamental frequency band. As PI requires the transmit of two pulses, the frame rate decreases. Moreover, it suffers from tissue motion artifacts. Motion in between the two transmitted pulses gives linear propagated signals which are not completely cancelled. In this case, a filter to obtain the second harmonic frequencies is still required. [68, 69, 70] Ideally, the described methods completely distinguish UCA from its surrounding tissue. Originally it was assumed that tissue is completely linear, making full separation possible. However, due to non-linear propagation of an US wave, tissue does produce notable harmonic content. [71] Consequently, the harmonic frequency band will be contaminated making separation more delicate. [61, 67, 68] Nevertheless, harmonic imaging and especially pulse inversion techniques are still considered as a sensitive method for contrast detection and widely used. [68, 72]

In an early phase of the clinical echo PIV trial performed at the Rijnstate hospital, discussed in Chapter 4, a combination of PI with frequency filtering was implemented for real-time UCA visualization. After the addition of PI to a three angled PW US acquisition scheme, used for anatomical navigation, bubbles were clearly visible. To further increase the contrast-to-background ratio (CBR) the scattered signal was high-pass filtered. However, this focus on the harmonic content caused an unexpected decrease in CBR. Further analysis revealed better bubble visualization when the scattered signal was not filtered or low-pass filtered. Therefore, the question arose if the currently used US settings are most optimal for real-time UCA visualization and if their is an underlying mechanism which could clarify the observation. This issue called for a better understanding of bubble behavior under different US conditions. To try to find an explanation for the observed increase in CBR when focusing on the fundamental frequency, in vitro experiments were proposed. These experiments and its results will be further discussed in this chapter.

3.2 Methods

Bubble behavior was investigated by performing in vitro experiments and hydrophone measurements at the University of Twente. The experimental setting gave the freedom to investigate different US settings. Several considerations, such as influences of temperature and viscosity, were made during preparation to limit the deviation between in vitro and in vivo settings. In the end, data of one patient was similarly analyzed to be able to compare in vitro to in vivo results. Hydrophone measurements were performed in order to quantify the acoustic pressure output.

Experimental set-up

A flow phantom of the femoral bifurcation was constructed using polyvinyl alcohol (PVA). PVA was chosen because of its matching acoustic properties to human tissue. [73] The PVA phantom consisted of a mixture of ethylene glycol and demineralized water, in a percent by weight (wt%) ratio of 40:60, and 12 wt% PVA (MW 85.00-124.00; 99%, hydrolysed) Cryogel (Sigma-Aldrich, Zwijndrecht, the Netherlands). During the final minutes of mixing scatterers (1 wt%, SiC Kiesgel 60, 0.0063-0.100 mm, Boom B.V., Meppel, the Netherlands) were added. A 3D printed vessel configuration with diameters of 8.9, 6.1 and 6.2 mm for the CFA, PFA and SFA respectively, was placed in a mold over which the PVA mixture was cast. The vessel configuration was placed at a depth of 20 mm. After three freeze-thaw cycles (at least 12 hours freezing and 8 hours thawing), the phantom reached a stiffness which was able to endure physiological pressures.
Subsequently, the phantom was placed in a controlled flow set-up, presented in Figure 3.1. A gear pump (KAVAN GmbH, Nürnberg, Germany) was used to enforce a steady, non-pulsatile, flow. A rigid pipe of approximately 20 cm, was connected to the inlet of the phantom to allow the formation of a laminar flow profile. The effect of the pump on the microbubbles is unknown. Therefore, the pump was placed at the outlet of the model, i.e. the flow was 'pushed' through the phantom, to establish a constant environment up to the scanning window at the CFA. The pressure was regulated with an external pressure regulator connected to the entirely sealed metal reservoir. By altering the pressure, the ambient pressure in the box, and consequently the pressure in the system, changed. The pressure was monitored using a manometer connected to a compliance chamber.
Microbubbles behave differently in room versus body temperature. [74, 75] Therefore, the experiments were carried out with the circulating fluid at a temperature of ∼37 degrees Celsius. Blood mimicking fluid (BMF) composed of glycerol (MW 92.094, 99.5%; Thermo Fisher Scientific, Waltham, MA, USA) and phosphate buffered saline (Gibco, Sigma-Aldrich, Zwijndrecht, the Netherlands) was used as circulating fluid in a ratio of 55:45 wt% to match physical properties of blood. This ratio considered the non-linear relation between temperature and viscosity of glycerol. [76] First, the BMF was preheated to ∼37 degrees Celsius after which it was degassed for 1 hour in the vacuum pump (Duran, DWK life Sciences GmbH, Mainz, Germany). Next, the BMF was placed in a water bad at a temperature of 37 degrees Celsius for at least 3 hours to restore gas equilibrium with the surroundings. During the experiments the metal reservoir was placed on a hot plate (IKA RCT Basic, IKA-Werke GmbH & Co., Staufen, Germany). A temperature sensor (IKA ETS-

D5, IKA-Werke GmbH & Co., Staufen, Germany) was inserted in the BMF in the metal reservoir. Through a feedback loop between the temperature sensor, set at a control value of 37 degrees Celsius, and the hot plate the temperature could be controlled throughout the experiments.

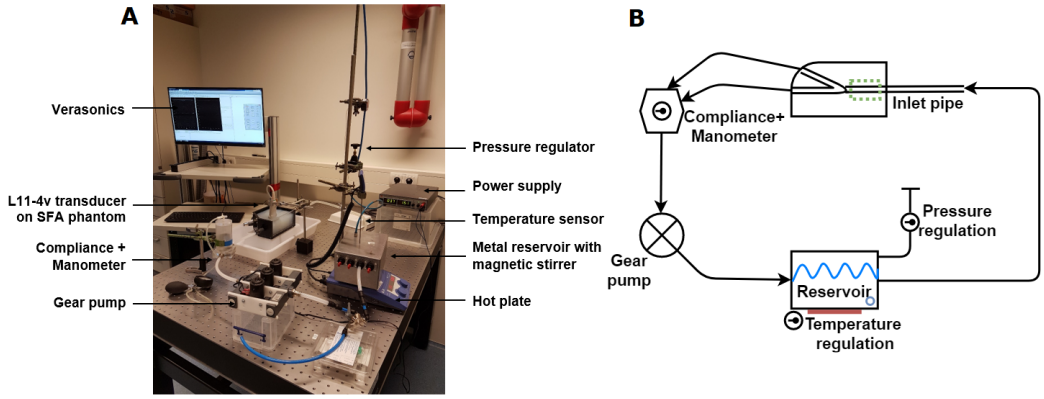

Figure 3.1: *Experimental flow set-up.* ***(A)*** *Image of the set-up with different parts labeled.* ***(B)*** *Corresponding schematic of the set-up. The green dashed square represents the scanning window.*

Microbubbles

Sonovue (Bracco, Milan, Italy) microbubbles were used as UCA with a concentration of 8 μL/ml. These microbubbles consist of a phopholipid monolayer filled with sulfur hexafluoride gas. The diameter of Sonovue ranges between 1-10 μm, with a mean diameter of 3 μm. More than 90% of the bubbles are smaller than 8 μm. Figure 3.2 presents the power spectral density (PSD) of Sonovue at two different acoustic powers. The resonant frequency is found around 3.4 MHz. When insonated with a higher acoustic power, a peak at the harmonic frequency appears. [60]

Data acquisition

Radio frequency (RF) data were acquired with a linear array transducer (L11-4v) connected to a research US system (Verasonics Inc, Kirkland, WA, USA). Characteristics of the transducer and used imaging parameters are listed in Table 3.1. The US system, including transducer, and programmed sequences were the same as used in clinical echo PIV measurements (Chapter 4). In short, for real-time UCA visualization a live view script is used in which a non-inverted and inverted single cycle PW US pulse is transmitted in three different angles. These six acquisitions are reconstructed into one image frame. The received signal was sampled at a rate of 32 MHz. The transmit frequency was set to 4.032 MHz and images were captured at 100 frames/s.
The influence of transmit voltage and pulse length on bubble behavior was investigated during three different flow conditions. Details of the different flow settings are given in Table 3.2. During each flow condition the transmit voltage was increased from 5 till 50V

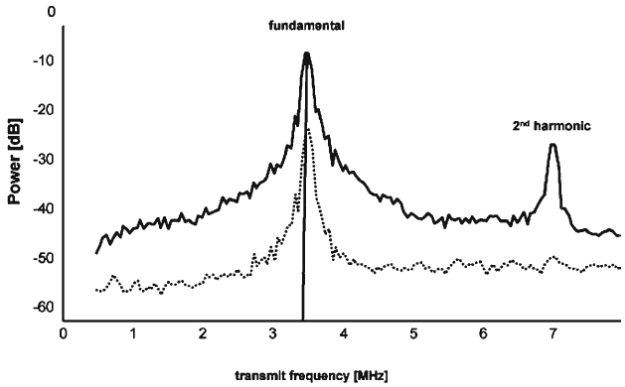

Figure 3.2: *Power spectral density of Sonovue at low (dashed) and high (solid) acoustic power. The backscattered signal presents a clear peak at the fundamental resonant frequency of Sonovue. When insonated with higher acoustic power a peak at the second harmonic frequency appears. Reproduced from E. Quaia. [60]*

with a pulse length of 1 or 2 cycles. Thus, in total six sets of measurements were carried out. The exact transmit voltages are given in Table 3.1. For each transmit voltage a live view recording of 2 seconds, i.e. RF data to reconstruct 200 frames, was saved as a binary file.

During each set of measurements 1.5L of BMF circulated through the flow set-up. Each time 0.6 mL of Sonovue was administered into the reservoir. A magnetic stirrer at 350 RPM ensured equal distribution of the UCA over the circulating fluid. Once the bolus passed and a constant passage of bubbles was visually established, a round of measurements was performed. To ensure a constant UCA concentration whilst increasing the transmit voltage, the BMF was redirected into a second container instead of recirculated into the reservoir. In between sets of measurements the circulating fluid was replenished and insonated with a continuous 50V HFR US pulse for at least 5 minutes to destruct all residual UCA. The BMF is likely to be contaminated with small air bubbles and/or dust. Therefore all measurements were performed before and after UCA was administered.

Table 3.1: *Specifications of the Verasonics L11-4v linear array transducer [77] and used imaging parameters for the live view (pulse inversion) sequence.*

Transducer parameter		**Imaging parameter**	
Center frequency	6.250 MHz	Transmit frequency	4.032 MHz
Number of elements	128	Imaging mode	Plane wave
Frequency bandwidth	4-11 MHz	Compounding angles	3
Elevation focus	15-25 mm	Angle range	36°
Pitch	0.3 mm	Frame rate	100 frames/s
		Excitation pulse	1-2 cycle sinusoidal
		Transmit voltage	5, 10, 15, 20, 30, 50 V

Table 3.2: *Flow parameters of the three different steady flow conditions.*

Flow condition	Flow (L/min)	Velocity (cm/s)	Pressure (mmHg)
Low	0.12	6.6	40
Diastolic	0.60	33.1	70
Systolic	1.32	72.9	100

Data analysis

The RF data of each measurement was analyzed using MATLAB R2018b (Mathworks, Natick, MA, USA). After loading the binary file into the workspace the data was reshaped into its original 3D form [samples, elements, frames]. By knowing the maximum acquisition length, wave length and number of samples per wave, the individual acquisitions could be identified. Per individual element all acquisitions were summed together, hence manually performing PI and coherent compounding of the three angles.
Subsequently, every 10th frame was analyzed in the frequency domain. Not the full imaged depth was of interest. Therefore, two regions were selected to represent the vessel and tissue. Figure 3.3 shows these regions of interest in a reconstructed US image. Per element, the signal parts corresponding to the selected depths were acquired. Finally, all signal parts were arranged in line resulting in an individual signal to represent the vessel and one to represent the tissue. These signals were the input for the frequency domain analysis.
An estimate of the PSD was computed using the pwelch function of MATLAB. This method used a moving hanning window to divide the signal in smaller epochs of which the FFT was computed. The windows had an overlap of 50%. The PSD was calculated as the average FFT over all windows. Figure 3.4 gives an example of an average PSD of one analyzed data-set. The peak of the transmit frequency (around 4-5 MHz) and the peak of the second harmonic frequency (around 8-9 MHz) were detected and analyzed for all measurements.
The influence of PI was investigated by comparing the frequency content of an individual inverted and non-inverted acquisition to the sum of both.

In vivo data

RF data of one patient, enrolled in the clinical echo PIV trial performed at the Rijnstate hospital (Chapter 4), were saved using the live view sequence at transmit voltages of 5, 10 and 20V with a pulse length of 1 cycle. Similar frequency analysis was performed on these data sets. Beforehand all systolic frames, in which the UCA was clearly visible, were manually selected. This resulted in less total frames and therefore every 3rd frame was analyzed instead of every 10th frame. Furthermore, due to the presence of a stent in the part imaged by the second half of the elements, only the first half was selected to obtain the regions of interest. An example of a frame and corresponding regions of interest is presented in Figure 3.3. The microbubbles are still visible in the stented region, however, the interference of the stent is unknown and investigating this lies outside the scope of this chapter.

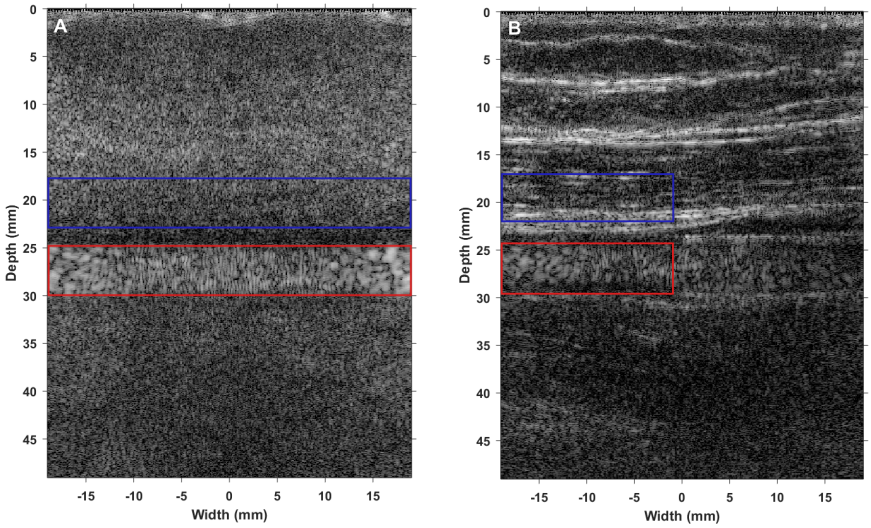

Figure 3.3: *Regions of interest selected to obtain a representative signal of a tissue part (blue box) and the vessel (red box) for further frequency analysis.* ***(A)*** *Reconstructed ultrasound image of the phantom, after pulse inversion was performed. The image was captured during diastolic flow conditions.* ***(B)*** *Reconstructed ultrasound image of a patient, after pulse inversion was performed. Both images are acquired with a transmit voltage of 10V and a pulse length of 1 cycle. Images are displayed at 40 dB dynamic range.*

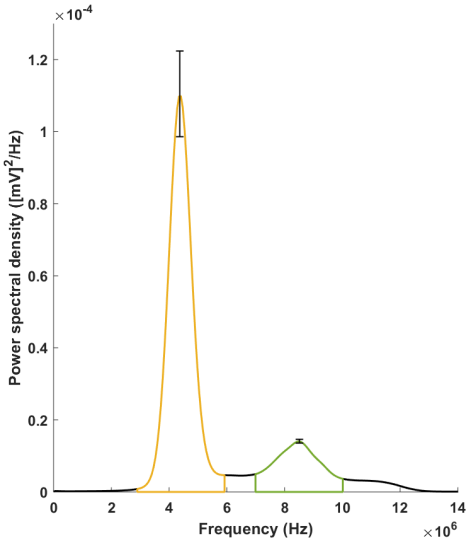

Figure 3.4: *Example of an average power spectral density of the 20 analyzed frames of one data-set acquired with a transmit voltage of 5V and a pulse length of 2 cycles. The fundamental and second harmonic frequency peaks are presented in yellow and green, respectively. The error bar shows the standard deviation of the peak intensity over the 20 analyzed frames.*

Hydrophone measurements

Hydrophone pressure measurements were performed to obtain the mechanical indexes (MI) of the US wave at the different transmit voltages. Previous hydrophone measurements with the L11-4v transducer at a transmit voltage of 50V showed an MI of 0.97 [78]. For most probes a linear relation between transmit voltage and MI applies. Therefore, hydrophone measurements were performed at a transmit voltage of 5V to test this linear relation. If linearity was proven, the remaining MI were calculated by means of interpolation.

3.3 Results

Hydrophone measurements of a volume scan with a transmit voltage of 5V showed an average MI of 0.06 at the depth of interest, 20-30 mm, with corresponding peak negative pressure of 150 kPa. Moreover, the maximum MI was 0.10. Hence, linearity is assumed and corresponding MI for all transmit voltages are (rounded to the nearest first decimal): 0.1, 0.2, 0.3, 0.4, 0.6 and 1.0.

During the in vitro measurements UCA was visible on the PI live view display under all varying conditions. Examples of reconstructed images, before and after administration of UCA, are given in Figure 3.5. These figures show a gradient between flow and contrast intensity. From the figures before UCA was administered, top row, it becomes clear that the BMF is highly contaminated.

Pulse inversion

Figure 3.6 shows frequency spectra calculated from the RF data in the vessel (left) and tissue (right) area. Figures 3.6A and B represent the inverted and non-inverted single acquisitions of different transmit voltages. In both vessel and tissue the single pulses overlay perfectly in the frequency band around the fundamental frequency, around 4-6 MHz. In the harmonic frequency band, around 8-10 MHz, the intensity is slightly different. This difference increases, from around 3 dB to 10 dB, with rising transmit voltages and is larger in the tissue region. After summation of the single acquisitions a clear suppression of the fundamental frequency can be seen in both vessel and tissue (Figures 3.6C and D). This suppression is higher (-80 dB) in tissue than in the vessel (-48 dB). From these figures it can be appreciated that after PI the fundamental frequency is more present in the vessel area compared to the tissue area. In the vessel area the intensity of the fundamental frequency is almost equal to the intensity of the harmonic frequency, whereas in the tissue area the intensity of the harmonic frequency is higher than the fundamental frequency.

Transmit voltage

The PSD was sucessfully obtained of all measurements for both the vessel and tissue signal. Figure 3.7 presents the mean peak values and standard deviation (shaded) of the fundamental (Fg, solid line) and harmonic (2nd, dashed line) frequency content, hereafter

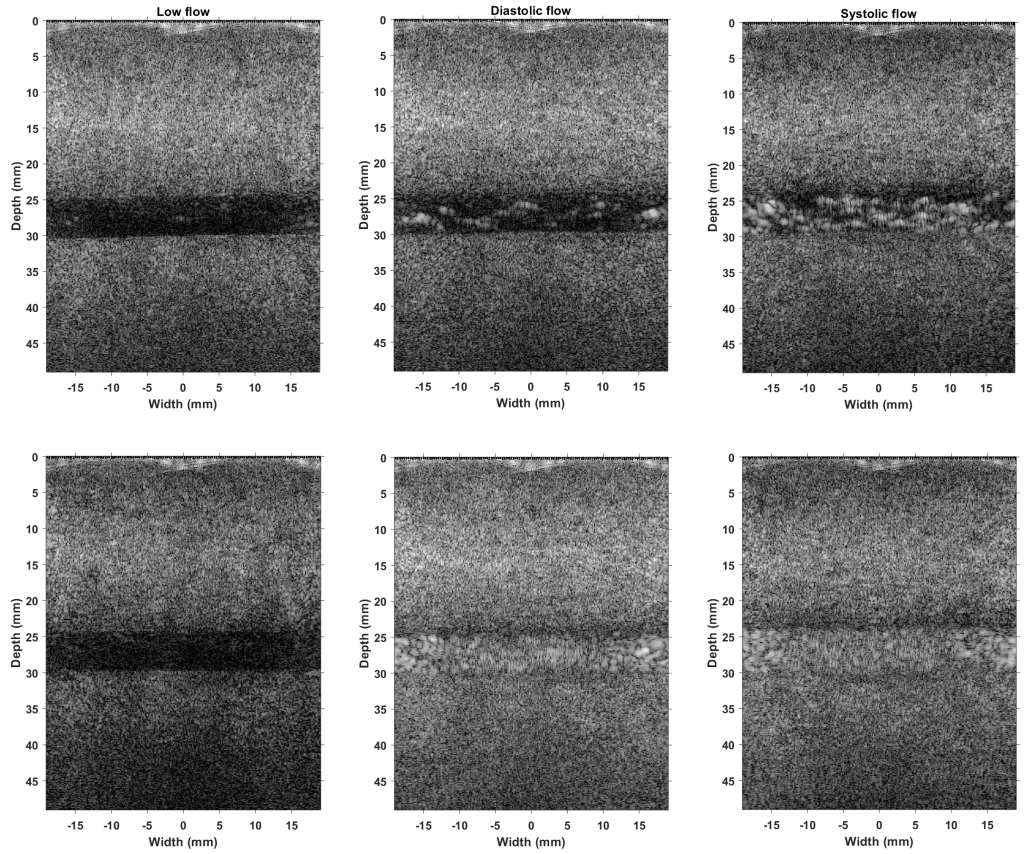

Figure 3.5: *Reconstructed ultrasound images of the phantom with increasing flow before (first row) and after (second row) microbubbles were administered. Flow increases from left to right. All images were captured with a transmit voltage of 15 V and a pulse length of 1 cycle. Images are displayed at 40 dB dynamic range.*

intensity, as function of the transmit voltage for the different flow settings. Results are shown for a pulse length of 1 cycle.

In general, intensity of the signal increases with increasing transmit voltage. The vessel and tissue signal show a comparable trend with increasing transmit voltage. Tissue shows the highest harmonic intensities compared to the vessel's contrast and baseline measurements, varying little between the different flow settings. The fundamental intensity of tissue shows little variation as well. In low flow conditions, the fundamental intensity of tissue is higher than the fundamental intensity of the vessel ROI. For higher flow, however, the fundamental intensity of the vessel region increases, becoming higher than the fundamental intensity of tissue. This increase is particularly noticeable for the vessel signals with contrast. Between diastolic and systolic flow conditions there is still an increase, however smaller. When only the fundamental frequency is considered, there is a clear difference between the baseline and contrast measurements. Especially in diastolic and systolic flow conditions. Harmonic intensity, however, is approximately equally present

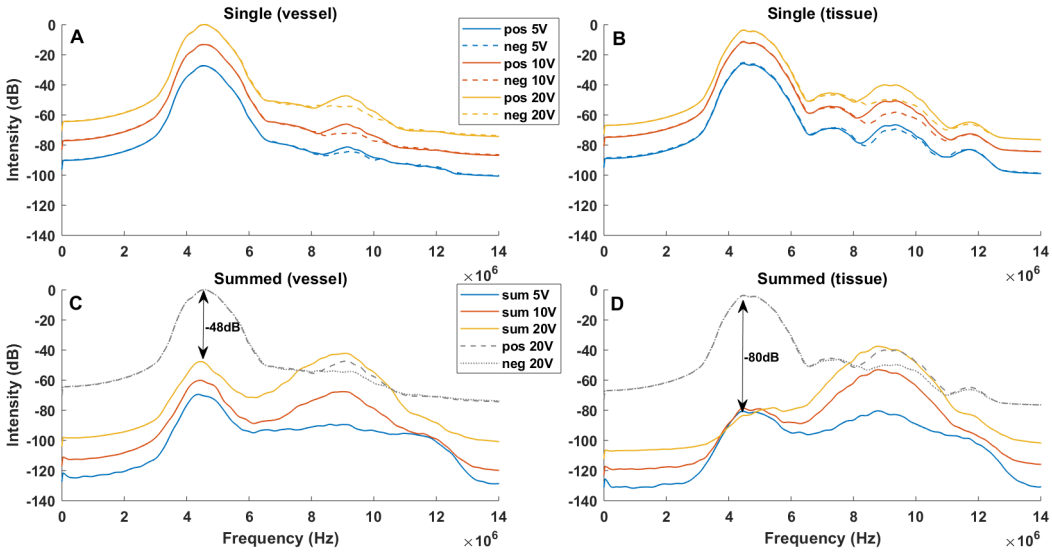

Figure 3.6: *The effect of pulse inversion on RF data in the frequency domain. All plots present data acquired during systolic flow conditions with a pulse length of 1 cycle. Intensity is given as function of frequency for a transmit voltage of 5, 10 and 20 V.* ***(A-B)*** *Received intensity from the vessel (A) and tissue (B) ROI of the individual non-inverted (pos) and inverted (neg) pulses.* ***(C-D)*** *The resulting intensity after summation of the inverted and non-inverted pulses for the vessel (C) and tissue (D) ROI. As a reference the intensities prior to summation, obtained with a transmit voltage of 20 V, are given in grey.*

and shows far less variations with increasing flow. In case of diastolic flow, the harmonic and fundamental intensities (contrast) intersect at a transmit voltage of 20V above which the harmonic intensity is higher than the fundamental intensity. When systolic flow is considered, this intersection shifted to a higher transmit voltage of approximately 40V.
The influence of pulse length on the fundamental and harmonic intensities is presented in Figure 3.8. This figure gives the results corresponding to a pulse length of 2 cycles. Baseline results are not shown. In general, a doubling of the pulse length results in an increase in harmonic intensity for both the vessel and tissue signal. This increase is less pronounced for the fundamental intensities. In comparison with a pulse length of 1 cycle the same trends can be noticed, such as the harmonic intensity of the tissue being the highest in all flows compared to the harmonic intensity of the vessel. A likewise intersection of the fundamental and harmonic intensities of the vessel region appears at 20V during systolic flow, where this occurs at 40V for a shorter pulse length.

In vivo data

Figure 3.9 gives the mean peak values and standard deviation of the fundamental and second harmonic intensities as function of the transmit voltage of the in vivo acquired live view US data. The overall intensity of the signal, both in vessel and tissue, is higher than the intensity of the signals obtained in the experimental set up. The harmonic intensity shows comparable results to the experimental data, being highest in the tissue signal. At

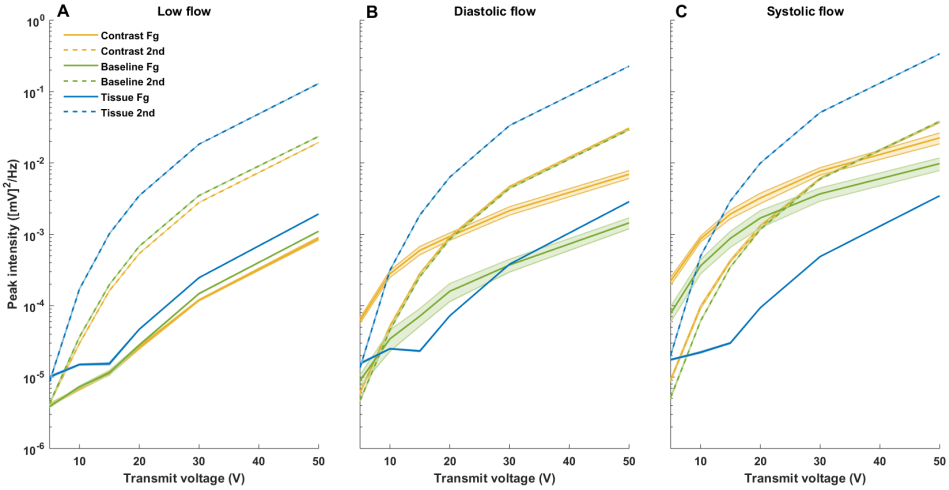

Figure 3.7: *The effect of transmit voltage and flow on the peak intensities of the fundamental (solid lines) and second harmonic (dashed lines) frequency for a pulse length of 1 cycle. All plots present peak intensity as function of the transmit voltage for the signals of the tissue and vessel region. The effect of the microbubbles is visualized by plotting the analyzed data of the vessel region before ('baseline') and after ('contrast') contrast agents were administered. Data is given for* ***(A)*** *low,* ***(B)*** *diastolic and* ***(C)*** *systolic flow. The shaded error bar shows the standard deviation of the peak intensity error.*

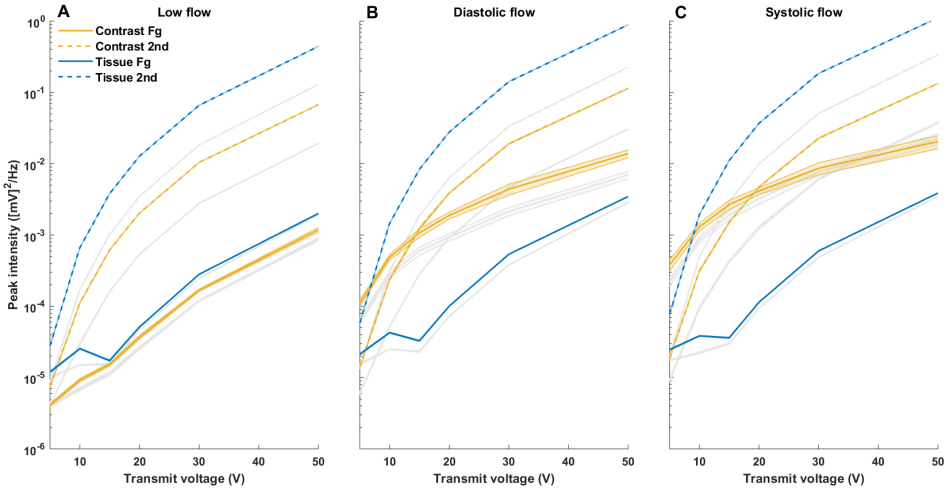

Figure 3.8: *The effect of transmit voltage and flow on the peak intensities of the fundamental (solid lines) and second harmonic (dashed lines) frequency for a pulse length of 2 cycles. All plots present peak intensity as function of the transmit voltage for the signals of the tissue and vessel region. Data is given for* ***(A)*** *low,* ***(B)*** *diastolic and* ***(C)*** *systolic flow. The shaded error bar shows the standard deviation of the peak intensity error. Baseline measurements are not considered. As a reference, results corresponding to a pulse length of 1 cycle are given in grey.*

a transmit voltage of 5V the fundamental intensity is higher in the tissue signal than in the vessel signal. At transmit voltages of 10 and 20V the fundamental intensity is equally present in the tissue and vessel signal.

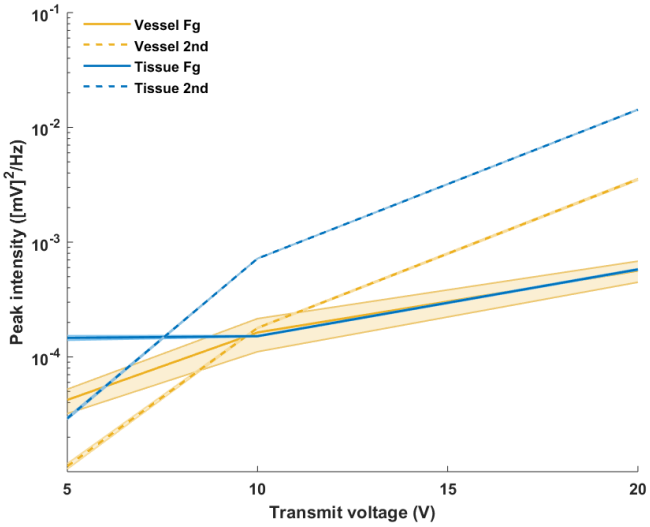

Figure 3.9: *The effect of transmit voltage on the peak intensities of the fundamental (solid lines) and second harmonic (dashed lines) frequency for in vivo acquired data. Mean peak intensities are given as function of transmit voltage for both the tissue and vessel region of interest. Presented results are obtained during systole, with a pulse length of 1 cycle. The shaded error bar shows the standard deviation of the peak intensity error.*

3.4 Discussion

In vitro experiments were successfully performed in a controlled flow setup. The influence of the transmit voltage and pulse length on bubble behavior was investigated by analysis of the frequency content of the RF data.
Analysis of the single acquisitions before and after PI, presented in Figure 3.6, showed a suppression of the fundamental frequency in both tissue and vessel, whereas the harmonic frequency content stayed unaffected. So, it seems that PI is working as intended. However, from the same figure it becomes clear that, especially in the vessel signal, there is still a noteworthy amount of fundamental left compared to the harmonic content. This is also emphasized in Figure 3.7 in which an increase in fundamental frequency is observed for all transmit voltages with increasing flow. This may indicate worsening of PI when flow increases. Such a residual clutter signal can originate from different sources as mentioned earlier, one of which is tissue movement. Because PI is a multipulse technique it is susceptible to motion. Dependent on the direction, the motion causes a time delay and/or changes the intensity of the received signals. [79] This decorrelation results in an imperfect cancellation of the linear signals. These so called tissue motion artifacts

are extensively discussed in literature. [68, 70, 79, 80] Shen et al. showed in a simulated model and experimental setting that the fundamental frequency becomes dominant in the PI sum when the displacement in axial direction is only 0.02 λ. In case of motion in the lateral direction, the fundamental becomes larger when the displacement is more than 0.3 times the beam width measured at focal depth. [79] These values are not directly applicable to the data acquired in this study, as plane wave US is used. Nevertheless, tissue motion is most likely the explanation for the higher fundamental signal intensities observed in the tissue region of the in vivo data compared to the fundamental intensities in the in experimental data. Although, the live view did not show a considerable amount of motion. The amount of fundamental intensity in the vessel signal of the experimental data relates to this phenomenon as well. It is the motion of UCA, working as linear scatterers, that causes the decorrelation between the two firings. This explains the increase in fundamental intensity with increasing flow. It also clarifies why better results of bubble visualization were found when using a low pass filter during previous analysis.

The second harmonic signal intensity of the vessel ROI is less than expected, especially in contrast to the harmonic signal received from tissue. Harmonic intensities increase with increasing transmit voltage, however, approximately the same harmonic intensities are measured from baseline measurements. It is therefore unlikely that this harmonic content originates from non-linear behavior of the microbubbles. The lack of harmonic signal from the UCA was unexpected. It is most probable that the UCA is not showing non-linear behavior because of unsuitable US settings. Microbubbles tend to show non-linear behavior when insonated with low acoustic power (peak negative pressure between 100-600 kPa) at their resonant frequency. [60] The transmit voltages until roughly 20V showed an acoustic power well within this range. For instance, 5V had an average MI of 0.06 at a depth of 20-30 mm with a corresponding peak negative pressure of 150 kPa. The transmit frequency, however, is set at 4.032 MHz, whereas the resonant frequency of Sonovue is approximately 3.4 MHz. As showed in Figure 3.2 Sonovue is much less sensitive to a frequency of 4.032 MHz. The ideal resonant frequency is inversely related to the square of the radius of the microbubble. Sonovue uses a range of diameters and therefore it is possible that some of the microbubbles with a very small radius will show non-linear behavior. [60] This is, however, far from enough to really make a difference in the overall frequency content of the signal. The harmonic content will probably benefit from lowering the transmit frequency of the transducer. This could be easily tested in a similar experimental setting in which transmit frequency is the varying parameter. The frequency bandwidth of the L11-4v transducer is, however, limited for such an experiment. A similar probe with a lower frequency bandwidth would overcome this problem as well as using two separate probes to transmit and receive the signal.

Moreover, pulse length could be optimized. Longer pulse length results in a higher acoustic power of insonation. [60] Pulse length is determined by the number of cycles per pulse wave. In this chapter 1 and 2 cycles per pulse were compared and an increase in harmonic content was noticed for both tissue and vessel. Furthermore, using more cycles per pulse results in a narrowing of the bandwidth of the transmit frequency. The spectrum of the transmitted frequency has a 3 dB bandwidth defined by the center frequency divided by the number of cycles. This decreases the likelihood for overlap between the frequency

bands and improves discrimination between fundamental and second harmonic frequencies. Longer pulse length comes at the cost of axial resolution. This should be considered when settings are being optimized.

Finally, PI is currently used in combination with PW US acquisitions. These unfocused transmissions impose a uniform acoustic pressure which impairs the non-linear behavior of the bubbles. PI is therefore probably not the best approach to enhance non-linear signal content. Amplitude (or power) modulation (AM) is another multipulse technique which uses consecutive US waves with different acoustic levels. The response of the bubbles will differ for each AM acquisition. PW in combination with AM showed good contrast-to-background ratios in comparison with conventional line-scanning AM approaches. [72] A combination of PI and AM is considered one of the most sensitive contrast detection methods. [62, 72]

Nevertheless, second harmonic frequencies are present in the vessel and, especially, tissue signals. Different sources contribute to this harmonic content and are most likely the same for both signals. First, it could be non-negligible harmonic components which were present at the surface of the transducer prior to propagation. This may happen due to a large pulse bandwidth as mentioned before or the ultrasound system itself being non-linear. However, hydrophone measurements showed no harmonic content close to the transducer. Therefore it is unlikely that these sources are the cause of the non-linearity in the signal. Another possible cause is non-linear propagation of the US signal. When the acoustic wave propagates through tissue (-mimicking material) non-linear propagation occurs. The further the wave travels, the more it gets distorted. Distortion of the signal also depends on the medium it propagates through. Tang et al showed a much more significant non-linear propagation through a cloud of UCA insonated at their resonant frequency than through tissue-mimicking material. [71] In this context, the higher harmonic intensities in the tissue signal, under almost all experimental conditions, are an unexpected result. Especially because the tissue region was selected anteriorly to the vessel. However, at this point it also clarifies why discrimination between tissue and contrast remains a challenge. This becomes especially clear from Figure 3.3 in which tissue appears very bright relative to the contrast.

Future perspectives

At present, bubble visualization is possible due to the motion of the bubbles causing decorrelation between the two PI pulses. In vivo data, however, shows that this residual signal after PI is also equally present in tissue. To improve the discrimination between UCA and tissue, it would be better to move towards a method in which the UCA is optimally used, hence oscillating in a non linear manner. A first step would be to optimize the US settings and acquisition scheme of which different examples are already described. Similar experiments could be performed to investigate if changing these US settings will improve harmonic content in the vessel area relative to the harmonic content of tissue. If so, a CTR analysis could help in understanding if an increase in harmonic content really improves the discrimination between perfused tissue and UCA. Other approaches would be to let go of the second harmonic frequency and focus more on sub- or superharmonic fre-

quencies. These frequencies are less affected by harmonic generation of the underlying tissue. [61, 68, 81, 82] However, with these strategies the next challenge already appears with finding, or building, a transducer with appropriate bandwidth.

Results of these in vitro experiments may have direct implications for clinical trials using echo PIV to quantify blood flow in humans. Currently, the microbubbles are visible due to motion causing imperfect cancellation of the ground frequency in the vessel compared to the ground frequency of tissue. However, this mechanism is less pronounced in the in vivo analyzed data showed in Figure 3.9. In vivo the intensity of the fundamental frequency of tissue was higher or equal to the fundamental frequency of the vessel. Real-time bubble visualization is an important step during the echo PIV measurements. Therefore, the mentioned possible improvements should be explored in light of the clinical trial. Optimizing the use of microbubbles, e.g. employ their non-linear properties, will most likely improve in vivo data acquisition.

3.5 Conclusion

PI established real time UCA visualization in both in vitro and in vivo acquired data. The mechanism behind this is most likely based on decorrelation due to motion of the UCA causing imperfect cancellation of the fundamental frequency, rather than non-linear properties of the microbubbles. Tissue shows a significant amount of harmonic frequencies, making discrimination between contrast and tissue based on the second harmonic frequency very difficult. Methods to improve non-linear behavior of the contrast should be further investigated.

4 Clinical feasibility of echo PIV

4.1 Introduction

The relation between local blood flow patterns and atherosclerotic plaque formation has been discussed in Chapter 1. Successful blood flow quantification may provide an important step towards being able to predict atherosclerotic disease progression. Furthermore, it may advance endovascular treatment on a patient specific level. The impact of significant changes in vessel geometry and local blood flow has been confirmed by recent observations in a randomized clinical trial, comparing heparin-bonded expanded endografts to a conventional femoropopliteal bypass. In both study arms, a concomitant endarterectomy of the CFA was a predictor for success resulting in better patency rates. This suggests that plaque removal, i.e. changing the vessel geometry, of the CFA could positively influence the flow characteristics at the inflow area of the stent or bypass. [42] This example elucidates once more the relation between local blood flow and progression of disease and stent patency. Furthermore, it emphasizes the importance to gain insight in these local flow patterns.

High-frame-rate contrast-enhanced ultrasound particle image velocimetry, in short echo PIV, proved to be a reliable method to quantify flow characteristics in the abdominal aorta and carotid artery in healthy volunteers. [10, 49, 83] This technique has never been used in the femoral trajectory. Moreover, its efficacy near stents is unknown. The objective of this study was to determine the feasibility of spatial and temporal blood flow quantification in the femoral bifurcation and near stents in the SFA using echo PIV. As this study is still ongoing, the aim of this chapter is to present the preliminary results.

4.2 Methods

This study has been performed at the Vascular Center of the Rijnstate Hospital in Arnhem, the Netherlands. The study was conducted in accordance with Good Clinical Practice guidelines and was approved by a central and local medical ethical committee in the Netherlands (NL65760.091.18).

Study design

This ongoing multidisciplinary single center exploratory study is performed with a prospective study design. There were no follow-up moments included. Procedures and treatment were executed per institutional protocol and standard of care for PAD.

Table 4.1: *In- and exclusion criteria.*

Inclusion criteria	Exclusion criteria
• Scheduled endovascular treatment of a lesion in the SFA by placement of a bare metal or a covered stent • A recently (<6 weeks) treated lesion in the SFA by placement of a bare metal or a covered stent	• Hypersensitivity to the active substance(s) or any of the excipients in Sonovue • hypersensitivity to iodinated contrast media • Clinically unstable cardiac disease, congestive heart failure (class 3/4), right-to-left cardiac shunt or prosthetic valves • Uncontrolled systemic hypertension • Hypercoagulable status, recent thrombosis • Severe pulmonary hypertension (pulmonary artery pressure > 90mmHg) • Severe pulmonary disease (e.g. COPD GOLD 3/4, ARDS) • Loss of renal function (GFR < 31ml/min) • End-stage liver disease • Sepsis • Pregnancy

SFA; superficial femoral artery, COPD; chronic obstructive pulmonary disease, GOLD; Global initiative for obstructive lung disease, ARDS; acute respiratory distress syndrome, GFR; glomerular filtration rate.

Study population

PAD patients with a stenotic lesion or occlusion of the SFA, recently (<6 weeks) treated with a stent placement or scheduled for a stent placement, were approached for enrollment. Both type of stents used in the SFA, bare nitinol (Everflex, Medtronic, Minneapolis, MN, USA) and covered nitinol (Viabahn, Gore Medical, Flagstaff, AZ, USA), were included. Patients were included after providing written informed consent. Patients who met one of the exclusion criteria listed in Table 4.1 were excluded from the study. A pilot of in total 20 PAD patients has been chosen. This is not substantiated with any power calculations.

Data acquisition

Echo PIV measurements were performed with a linear array transducer connected to a fully programmable Vantage 256 US machine (L11-4v transducer; Verasonics, Kirkland, WA, USA). Transducer specifications can be found in 3.1. HFR US data were acquired in five different locations around the femoral bifurcation and the stented lesion. These locations were the CFA, PFA, bifurcation, proximal edge of the stented SFA (inflow) and

distal edge of the stented SFA (outflow). A schematic representation of the locations is given in Figure 4.1.
First, proper visualization of the vessel was established by an experienced vascular technologist, using a clinical US machine (iU22 xMATRIX, Phillips Healthcare, Best, the Netherlands). Blood flow velocities were measured using pulsed wave Doppler, after which the switch was made to the research US machine. This system uses the same real-time, live view, visualization sequence as explained in Chapter 3. For anatomical navigation a three angled PW, 1 cycle, acquisition scheme at 100 frames/s was used. After compounding and reconstruction the images were displayed real-time. A similar US scheme, with the addition of PI, ensured bubble visualization at a second display. For these live view acquisitions transmit frequency was set to 4.032 MHz and transmit voltage varied between 5 and 20 V. When sufficient visualization of all locations was established once more, venous access was obtained by placing a venous cannula.

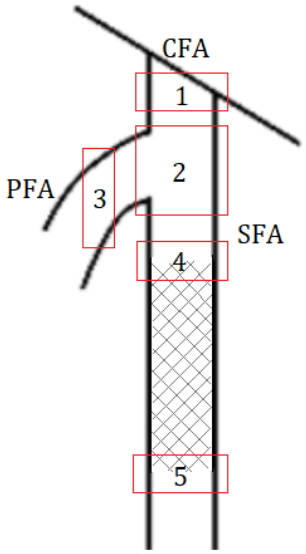

Figure 4.1: *Schematic of the femoral trajectory with all measured echo PIV locations highlighted in red. The locations are, in ascending order, the common femoral artery (CFA), the bifurcation, the profunda femoral artery (PFA), the proximal edge of the stent in the superficial femoral artery (SFA), i.e. inflow, and the distal edge of the stent in the SFA, i.e. outflow.*

Sonovue was used as a contrast agent in a concentration of 8 μl/ml. Sonovue is clinically approved for applications in radiology and cardiology in the European Union. [59] The suspension was prepared following the attached recipe. In the environment of the vial the microbubbles are stable for several hours. However, buoyancy causes the microbubbles to rise to the surface in less than 2 minutes. Before intravenous injection the vial was agitated slowly in a top-to-bottom manner to once more obtain a homogeneous suspension. Sonovue has a half-life time of 6 minutes. After intravenous injection, more than 80% of the suspension is exhaled through the lungs in 11 minutes. [84] More specifics on US prop-

erties of microbubbles in general and Sonovue can be found in Chapter 2 and Chapter 3, respectively.
For each location 0.75 ml of Sonovue was injected. Generally, the bolus of contrast appeared within 20-40 seconds. When a semi-stable concentration of contrast was established a live view measurement was saved, followed by two HFR measurements. For each HFR measurement a three-angled PW, 1 cycle, acquisition scheme was used to capture images for 2.5 seconds at 2000 frames/s. Transmit frequency remained 4.032 MHz and transmit voltage was set to 5 and 10 V. To avoid accumulation of bubble concentration, an interval of several minutes was implemented in between measurement locations. When visually all UCA seemed cleared on the live view PI display, the next location was visualized and microbubbles were injected again.
Beside the echo PIV measurements, a CTA was carried out to provide insight into the lesion characteristics and to obtain the patient-specific geometry of the vessels for reference.

Data analysis

Echo PIV data were processed offline using MATLAB R2018b. First the RF data were clutter filtered based on singular value decomposition (SVD). [85, 86] The data were rearranged into a 2D space-time Casorati matrix. Subsequently, this matrix was decomposed using SVD causing tissue, which has a high spatiotemporal coherence, to gather in the low-rank modes of the system, i.e. described mainly in the first singular values. Flowing microbubbles in the blood, on the other hand, exhibit much lower spatiotemporal coherence and were typically distributed more centrally. High-rank modes were occupied by noise. Modes to truncate the diagonal matrix of singular values were chosen manually, based on visual inspection of the data. Low ranks ranks varied between 150 and 200, whereas high ranks varied between 1500 and 2200. After sufficient tissue suppression was achieved, without affecting the microbubbles during (very) low flow, the RF data were reconstructed into image data by the research US system. This beam formed image data was used to perform PIV analysis.

PIV analysis

PIV analysis was performed in an iterative manner with progressive grid refinement. Four iterations of blockwise cross-correlations were calculated between each image pair. A final 32 x 32 (pixel) interrogation window with 75% overlap was used, corresponding to a final spatial vector grid of 0.76 x 0.76 mm^2. For each iteration 2 x 3 (pixel) parabola peak fitting and median outlier detection [87] were used to estimate the sub-pixel displacement and eliminate erroneous vectors, respectively. By means of inter- and extrapolation of the resulting estimations from the previous iteration, a displacement predictor is made to linearly deform the images for the next iteration. The final correlation maps of five consecutive frames were averaged and the maximum normalized cross-correlation per window was used to determine velocity vectors. During post processing velocity vectors based on a correlation value < 0.1 were removed. Per vector field, a similar universal median outlier detection was applied. Furthermore, vectors deviating more than 4 times the standard

deviation were eliminated. All removed velocity vectors were interpolated. Finally, a 3 x 3 (pixel) Gaussian filter was applied to spatially smooth the acquired velocity data.

Feasibility

In order for PIV to properly be able to analyze contrast-enhanced US images, several features are considered to be important: to what extent the vessel is visualized and the ability to distinguish the imaged vessel, i.e. the intensity of the contrast agents. Therefore a first approach in assessing feasibility of echo PIV was performed by evaluating the data, obtained with a transmit voltage of 10V, in three steps.
The first step yielded an evaluation of the imaged vessel of all acquired data-sets. Based on an average image, derived from 20 frames during systole, the data was considered poor, medium or good. Examples are given in Table 4.2 figures A-C. An image was considered good when a clear outlined vessel could be appreciated over a length of at least three times the diameter (Figure C). When the vessel contained considerable shadows or void regions the data was valued medium (Figure B). Poor meant almost no vessel visible or only partly visible with no relevant anatomical information (Figure A).
During the second step the contrast-to-background ratio (CBR) was calculated of the same 20 frames, defined as:

$$CBR = 20log_{10}\frac{\overline{RMS}_{contrast}}{\overline{RMS}_{background}} \tag{4.1}$$

with $\overline{RMS}$ being the time averaged root-mean-square intensity of a selected contrast or background area. Three regions inside the vessel were selected, hence the influence of shadow and void regions was taken into account. The selected areas are highlighted in red (contrast/vessel) and blue (background) in the examples given in Table 4.2 figures D-F. The given examples were all considered having relatively good visibility of the vessel. Data considered as poor during the first step were not included in the second step.
Based on the obtained results from the first two steps, one patient was chosen to be evaluated in detail during the third step yielding PIV analysis. the maximum normalized cross-correlation maps were used to evaluate the accuracy of PIV. The median maximum normalized cross-correlation value with interquartile range (IQR) was calculated of the 20 analyzed frames. Furthermore, temporal velocity profiles obtained from PIV were compared to the results of Doppler duplex US. Both PSV and waveform morphology were assessed.

Transmit voltage

The influence of transmit voltage was assessed by calculating the CBR on a subset of 20 frames during peak systole and the end of diastole, comparing both transmit voltages of 5 and 10V. Furthermore, maximum normalized cross-correlation values were evaluated to assess the accuracy of PIV analysis. These calculations were performed on the data of the patient chosen for the detailed PIV analysis. The exact peak systole and end of diastole were obtained from the temporal velocity profiles acquired with PIV.

Table 4.2: *Examples of poor, medium and good vessel visibility* ***(A-C)*** *and bubble intensity* ***(D-F)*** *quantified by contrast-to-background (CBR) calculations.*

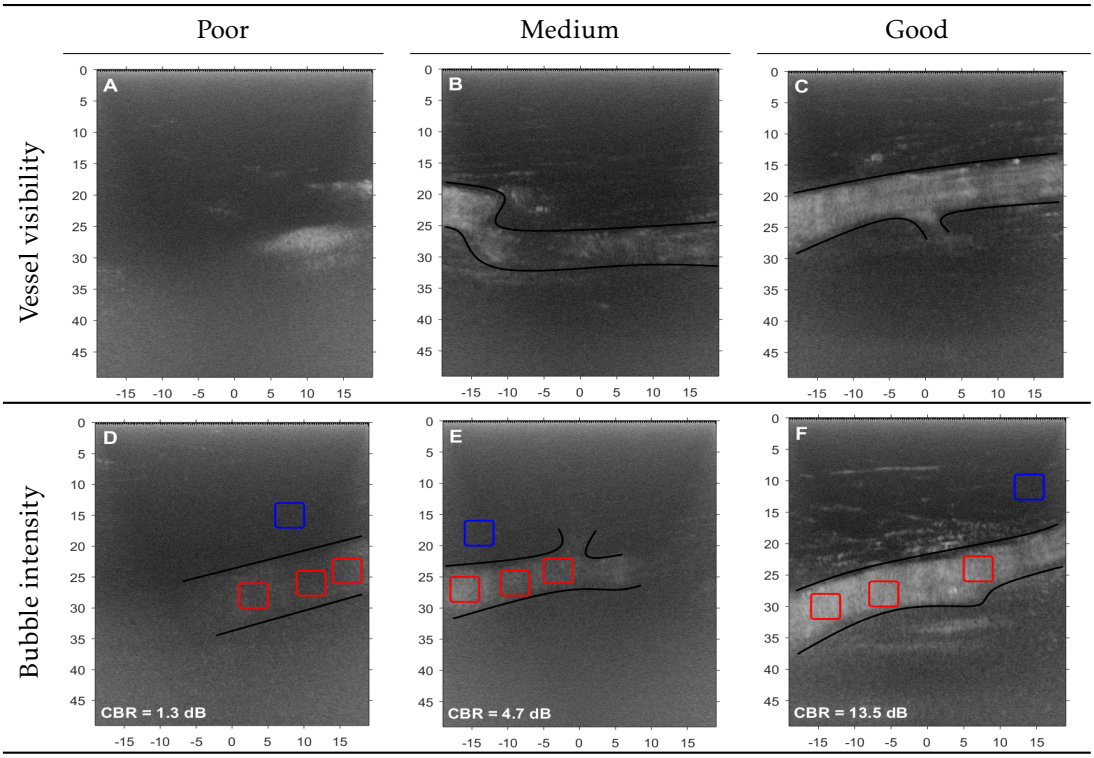

An average of 20 frames is displayed at 40 dB dynamic range. Axes are in mm.

4.3 Results

Nineteen patients have been enrolled to date. Echo PIV data was successfully acquired in twelve patients (10 male, 83.3%) with a median age of 68.5 years (IQR, 66.8;76.8). The seven remaining measurements are scheduled. Specifics of the used stent types and locations of the treated lesions are presented in Table 4.3. One patient was excluded, after physical examination with the clinical US device revealed an acute occlusion of the recently placed stent. Another patient received thrombolytic therapy prior to the stent placement, two months before the echo PIV measurement. None of the patients experienced side effects of Sonovue.

Table 4.3: *Stent specifications.*

Stent location		**Stent type**	
Proximal SFA, n (%)	2 (16.7)	Everflex, n (%)	6 (50.0)
Distal SFA, n (%)	2 (16.7)	Viabahn, n (%)	6 (50.0)
Mid SFA, n (%)	3 (25.0)		
Entire SFA, n (%)	5 (41.7)		

Feasibility

In total 60 sets of data were evaluated during the first step of feasibility assessment. 10 out of 60 locations showed poor vessel visibility with no relevance for PIV analysis. Half of the remaining 50 locations showed considerable shadow or void regions and were valued medium, leaving 25 locations with a clearly outlined imaged vessel. Patients showed large variation in imaged vessel dimensions between the different measured locations. All patients, except for one, had at least two locations in which the captured vessel was clearly visible.

The results of the CBR calculations are presented in Figure 4.2. From this figure it can be appreciated that, in general, medium scored vessels have a lower CBR ranging from -1.4-5.4 dB. Clearly visible vessels, scored with good in the first step, have on average a higher CBR, however, the distribution is larger ranging from 1.3-14.9 dB. CBR values differ a lot between and within patients. Seven out of twelve patients had at least two locations with sufficient vessel visibility and high CBR. One of these patients was used to further investigate the influence of transmit voltage and to perform PIV analysis.

Transmit voltage

The influence of transmit voltage on the CBR is presented in Figure 4.3. Examples of the outflow during diastole and systole are given in subfigures 4.3A and B, respectively. CBR is given for both systole and diastole with a transmit voltage of 5 and 10V. At a transmit voltage of 10V a higher CBR is found for all locations during systole and diastole. On average, a difference of 3.7 dB in favor of 10V is found. Both 5 and 10V show little

variation in CBR between systole and diastole. 5V shows a mean variation of 0.4 dB, whereas 10V shows a mean variation of 1.2 dB.

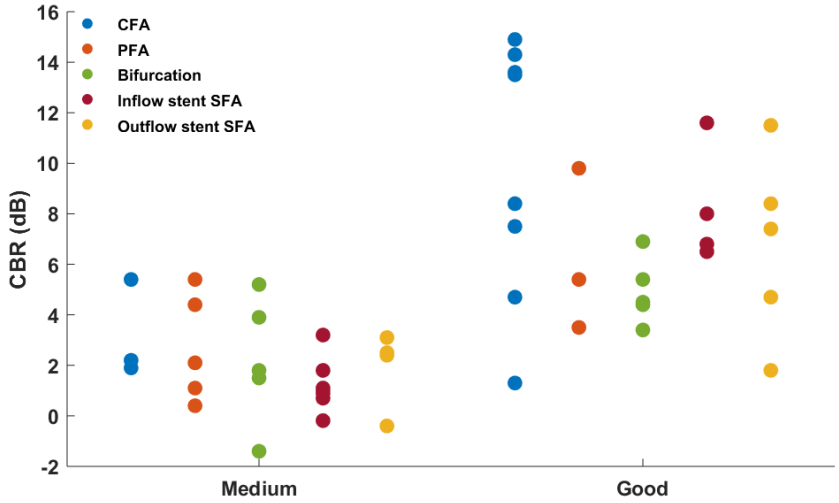

Figure 4.2: *Contrast-to-background ratios for all data with medium (left) or good (right) vessel visibility. Each colored dot represents an individual HFR measurement.*

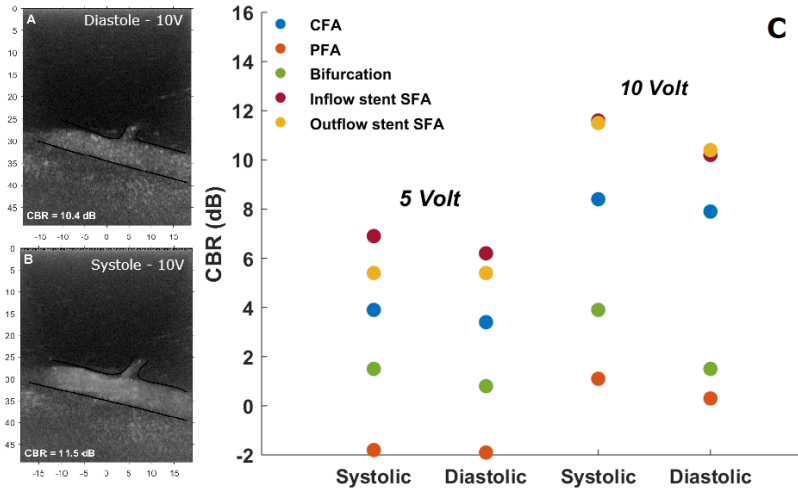

Figure 4.3: *The influence of transmit voltage on the contrast-to-background ratio during systole and diastole. Data of one patient is presented. An average of 20 reconstructed US images of the outflow of the stent are given as an example during* ***(A)*** *diastole and* ***(B)*** *systole.* ***(C)*** *CBR of all five locations with a transmit voltage of 5 and 10 V.*

Particle image velocimetry

CBR and PIV results of one patient are presented in Table 4.4. For each location the CBR, cross-correlation value and PSV obtained with PIV and duplex are given. In case of the CFA and inflow of the stent, PSV obtained with PIV corresponds well with PSV obtained with duplex. A relative difference of 9.2 and 0.9% is found for the CFA and inflow of the stent, respectively. These locations show high CBR together with relatively high median cross-correlation values. The outflow area of the stent shows a high mean CBR as well, however, the cross-correlation value is lower. The resulting difference in velocity is 25%. The locations with the lowest CBR and cross-correlation values, i.e. the PFA and bifurcation, show the least amount of agreement between PSV obtained with PIV and duplex.

The influence of transmit voltage on the cross-correlation values is presented in Table 4.5. In general, data acquired with a transmit voltage of 10V shows higher cross-correlation values than a transmit voltage of 5V. At both transmit voltages, a weaker correlation between frames is observed during systole.

To illustrate the difference in results from PIV analysis performed on data with low and high CBR, the bifurcation and the inflow of the stent are presented in full detail in Figures 4.4 and 4.5. Subfigures A and B show the vector field obtained with PIV and the

Table 4.4: *CBR and PIV results of one patient.*

Location	CBR (dB)	xcorr (a.u.)	PSV PIV (cm/s)	PSV duplex (cm/s)	Difference (%)
CFA	8.4 ± 1.3	0.46 (0.33;0.58)	107	118	9.2
PFA	1.1 ± 0.7	0.19 (0.09;0.32)	83	234	64.5
Bifurcation	3.9 ± 0.9	0.29 (0.18;0.42)	70	111	36.9
Inflow stent	11.6 ± 0.8	0.48 (0.31;0.60)	114	115	0.9
Outflow stent	11.5 ± 0.8	0.31 (0.21;0.42)	84	112	25.0

Contrast-to-background ratio (CBR) and cross-correlation value (xcorr) are presented as mean value followed by the standard deviation and median value followed by the inter-quartile range, respectively. CFA; common femoral artery, PFA; profundal femoral artery, PSV; peak systolic velocity, PIV; particle image velocimetry.

Table 4.5: *Cross-correlation values during systole and diastole for a transmit voltage of 5 and 10 V.*

Location	Systolic 5V	Diastolic 5V	Systolic 10V	Diastolic 10V
CFA	0.32 (0.22;0.43)	0.41 (0.32;0.51)	0.46 (0.33;0.58)	0.53 (0.40;0.64)
PFA	0.10 (0.07;0.15)	0.08 (0.06;0.14)	0.19 (0.09;0.32)	0.14 (0.08;0.28)
Bifurcation	0.29 (0.16;0.41)	0.48 (0.37;0.58)	0.29 (0.18;0.42)	0.22 (0.12;0.38)
Inflow stent	0.29 (0.16;0.41)	0.45 (0.34;0.57)	0.48 (0.31;0.60)	0.57 (0.47;0.65)
Outflow stent	0.17 (0.10;0.27)	0.37 (0.24;0.49)	0.31 (0.21;0.42)	0.56 (0.48;0.65)

Values presented as median followed by the interquartile range. CFA; common femoral artery, PFA; profunda femoral artery.

corresponding cross-correlation values inside the area of interest. In case of the inflow of the stent, especially the first half of the captured vessel exhibits high cross-correlation values. These values decrease inside the stented area. The duplex US image (Figure 4.4D) shows the temporal velocity profile at the proximal edge of the stent in the middle of the vessel lumen. Roughly the same point was taken in the obtained vector field to plot the velocity as a function of time, shown in Figure 4.4C. The obtained velocity profile corresponds well with the velocity profile of the duplex US. Both show similar triphasic waveform morphology. The bifurcation, captured as the transition of the CFA into the SFA, shows lower overall cross-correlation values and velocity seems to be underestimated (Figures 4.5A and B). This also becomes clear when comparing temporal velocity profiles, obtained at the proximal SFA. The velocity profile acquired from the PIV data seems a bit more noisy and shows lower PSV values compared to duplex US. The wave morphology is, again, approximately the same.
Figure 4.6 shows the resulting vector fields of the CFA during different instances of the cardiac cycle. PIV was able to obtain adequate vector fields during early systole, peak systole and diastole with median cross-correlation values of 0.39 (IQR, 0.29;0.51), 0.46 (0.33;0.58) and 0.53 (0.40;0.64), respectively.

4.4 Discussion

A first attempt in proving feasibility of echo PIV in the femoral bifurcation and near the stented SFA has been performed. Vessel visibility and CBR have been designated as key factors to quantify feasibility. Adequacy of PIV was evaluated using maximum normalized cross-correlation values and resulting velocities compared with duplex US. Results of one patient have been presented in detail and demonstrated that PIV was able to assess blood flow velocities during every phase of the cardiac cycle. As shown in Figures 4.4 and 4.6, a range of blood flow velocities was registered, including velocities up to approximately 110 cm/s and very slow rates approaching blood stasis. The acquired temporal velocity profiles corresponded well with the waveforms obtained with duplex US. Two out of five locations, i.e. CFA and inflow of the stent, showed a relative difference in PSV below 10%. These specific locations exhibited higher CBR and cross-correlation values in comparison with the locations performing worse. This indicates that PIV performs better when the acquired data has a high CBR. Considering this statement in context of all calculated CBR, presented in Figure 4.2 adequate PIV analysis is expected to be plausible in at least a quarter of the obtained echo PIV measurements. However, the deviating results of the outflow measurement of this one patient do not support this assertion. The outflow of the stent showed high CBR in combination with slightly lower cross-correlation values and underestimated the PSV with 25%. Therefore, a clear cut-off value for CBR, above which accurate PIV analysis is most likely to be accomplished, cannot be set based on the data of this one patient. More data should be analyzed through PIV to be able to make a justified statement about a certain threshold and to estimate the attributed value of CBR in pre-PIV screening.
Voorneveld et al. [83] found higher CBR values in their echo PIV data obtained in the abdominal aorta of healthy volunteers. They observed a similar decrease in CBR during

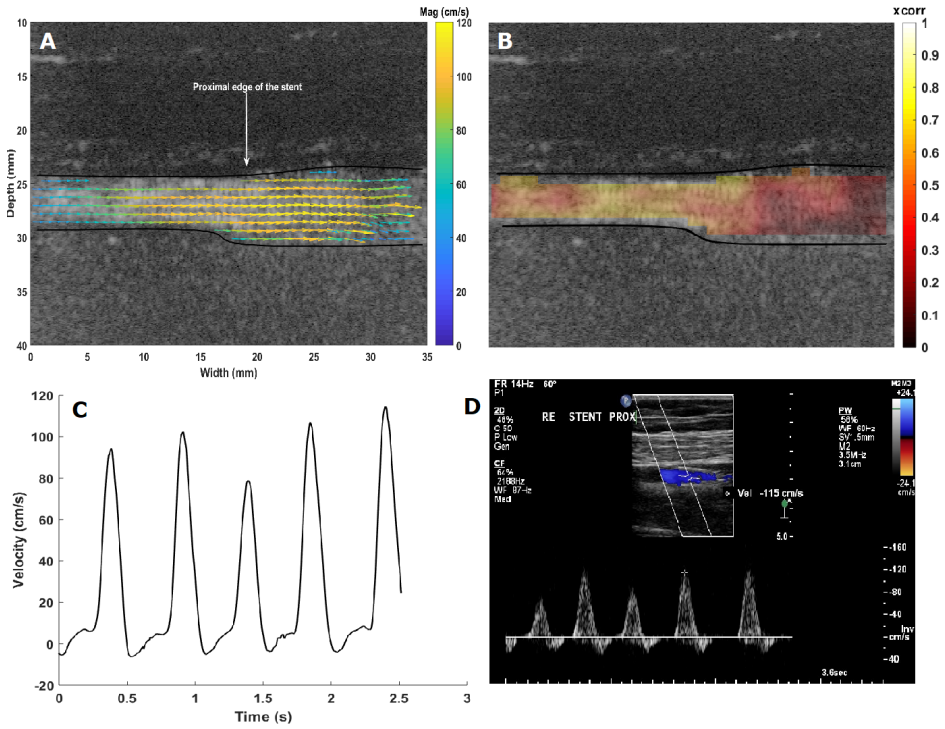

Figure 4.4: *Particle image velocimetry (PIV) results in the proximal edge of the stent in the SFA during systole. Data was obtained with a transmit voltage of 10 V.* ***(A)*** *Velocity vector field. Color represents the magnitude of the velocity vectors.* ***(B)*** *Cross-correlation values of PIV analysis. Color represents the maximum normalized cross-correlation value of the specific interrogation window.* ***(C)*** *Temporal velocity profile acquired at the proximal edge of the stent.* ***(D)*** *US duplex image of approximately the same location prior to the echo PIV measurements.*

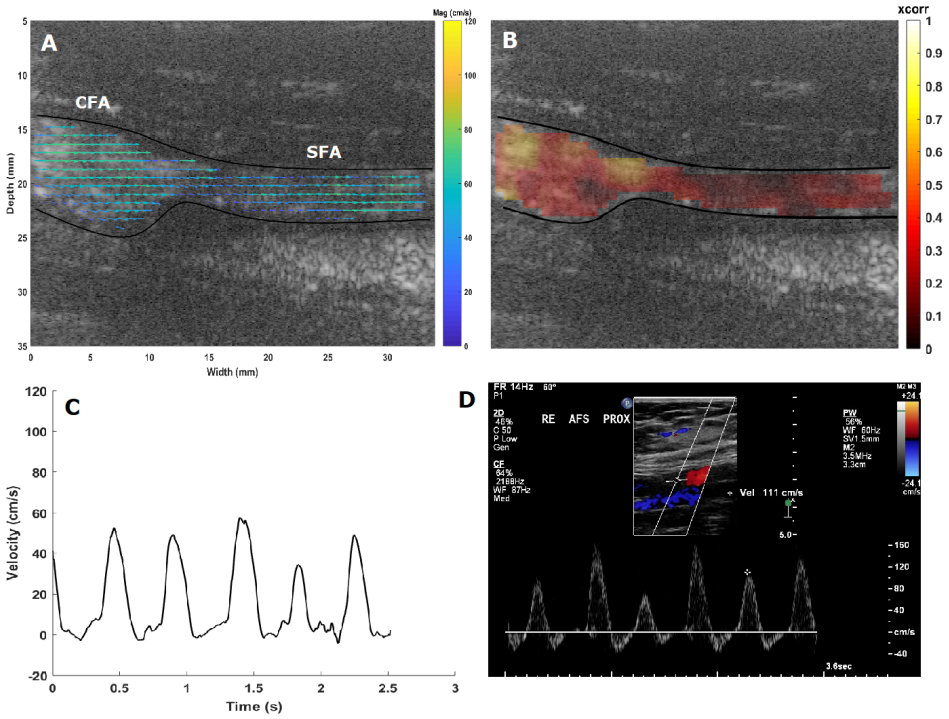

Figure 4.5: *Particle image velocimetry (PIV) results in the bifurcation during systole. Data was obtained with a transmit voltage of 10 V.* ***(A)*** *Velocity vector field. Color represents the magnitude of the velocity vectors.* ***(B)*** *Cross-correlation values of PIV analysis. Color represents the maximum normalized cross-correlation value of the specific interrogation window.* ***(C)*** *Temporal velocity profile acquired at the proximal superficial femoral artery.* ***(D)*** *US duplex image of approximately the same location prior to the echo PIV measurements.*

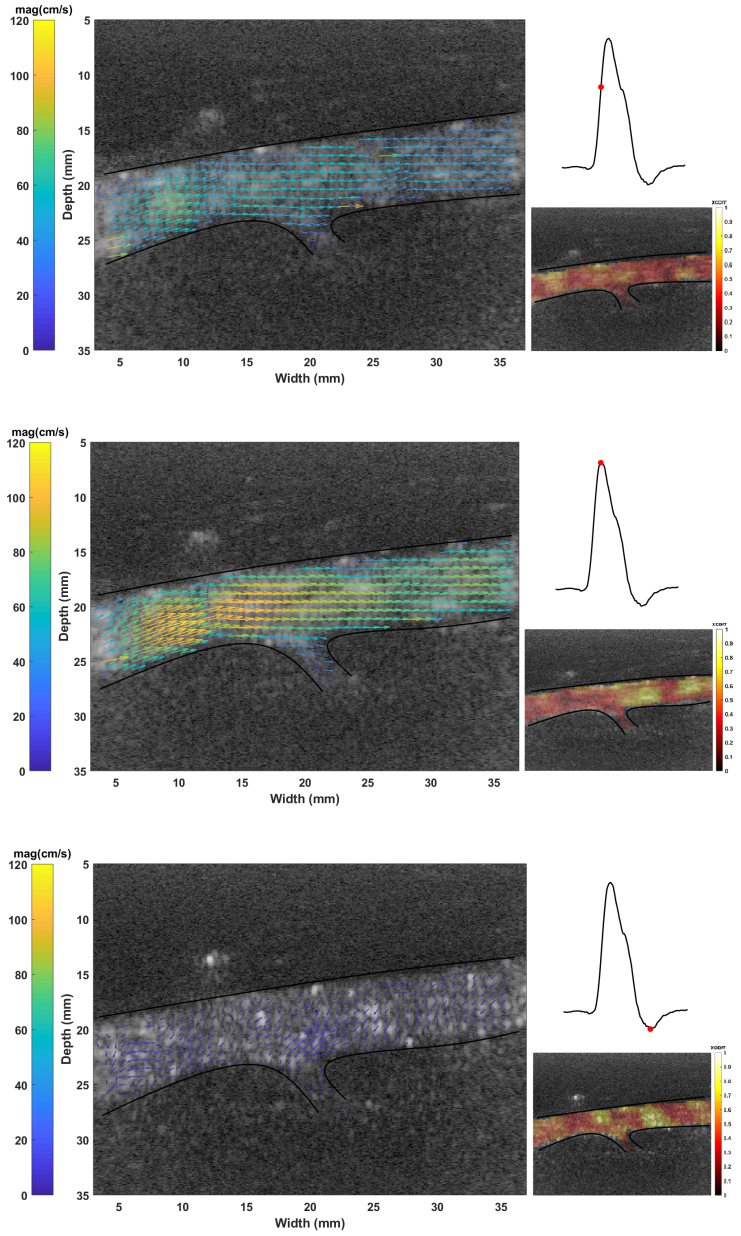

Figure 4.6: *Particle image velocimetry results during different instances of the cardiac cycle. The velocity vector field and corresponding cross-correlation value map is presented for (from top to bottom) systole, peak-systole and diastole.*

diastole (Figure 4.3). The difference in CBR could be explained by the difference in MI used in both studies. They indicated a maximum MI of 0.03, at a depth of interest of 30 mm, at which no severe bubble destruction occurred (during systole). The MI at 30 mm used in this study was higher; 0.06 and 0.12 for a transmit voltage of 5 and 10V, respectively. The higher MI could have caused significant bubble destruction, hence lowering the CBR. Severe bubble destruction will hamper PIV analysis and is hard to quantify visually. Therefore, bubble destruction should be investigated, for both transmit voltages, by calculating the disruption ratio. [62, 83] Moreover, the progressively diseased vessels of the patients measured in this study could be an explanation for the lower CBR. Calcifications at the anterior vessel wall cause shadows in the US image and impair vessel visibility. In such a case, average CBR will automatically be lower. However, obvious calcified lesions were not always visualized with the clinical or research machine and therefore it is unclear if this is the sole cause of the shaded regions.

Although lower CBR values were established, normalized maximum cross correlation values, listed in Table 4.4, correspond well with those reported by Voorneveld et al. This especially applies for the measurements of the CFA, inflow and outflow of the stent, showing higher cross-correlation values during systole relative to the values found in the abdominal aorta of healthy volunteers. [83] Hence, suggesting that comparable accuracy of PIV could be established. Based on solely the PSV values compared to the duplex US, accurate PIV results were obtained in the CFA and inflow of the stent. The outflow of the stent showed a larger deviation in PSV values. This could be due to overly smoothing of the data. For instance, velocities based on cross-correlation values < 0.1 were removed and interpolated. Furthermore, periods of fast flow showed weaker correlation between frames. This may cause difficulties for the PIV algorithm in tracking UCA during systole, in particular near stenotic lesions where flow velocities are expected to be even faster. Administering a smaller volume of contrast may ensure better correlation values during systolic flow. [83] The transmit voltage of 10V showed higher cross-correlation values compared to a transmit voltage of 5V, suggesting PIV to performs better on data acquired with a transmit voltage of 10V.

Unfortunately, these promising results were not observed in all measured locations of the patient discussed in detail. It seems that measurements with lower quality in terms of visibility of the imaged vessel and bubble intensity, PIV analysis performs worse. Several improvements can be made to optimize the quality of the acquired data, prior to PIV analysis. Enhancement of the images prior to PIV analysis will minimize the occurrence of spurious vectors in the PIV results. This is desired because not all spurious vectors are detected by the outlier algorithms and interpolation of the removed outliers introduces unknown errors. W. Thielicke [52] describes multiple pre-processing techniques which are used to enhance the images. These techniques include contrast limited adaptive histogram equalization, intensity high-pass filtering and intensity capping. [52, 88] Optimal settings of these filters and the influence on PIV results should be further investigated.

Furthermore, tissue suppression SVD based filtering is currently performed by choosing the modes manually by means of trial and error. Beside its time consuming and computational (work) load, it also increases variability of the measured data. Several automated selection algorithms have been described and applied on echo PIV data in other

studies. [83, 86] Such an algorithm will provide a method in which all data is objectively filtered in a similar way.
Moreover, bubble visualization could be improved by adding the PI technique to the HFR sequence, utilizing the non-linear behavior of the microbubbles. [50] However, the subsequent decrease in frame rate may impair the dynamic range over which velocities could be detected. Besides, if the microbubbles experience non-linear behavior during the HFR sequence remains questionable. Frequency analysis, like performed in Chapter 3, could provide insight in this case.
In addition to improvements of the quality of the measured data, PIV analysis itself could be optimized. When performing PIV analysis, numerous settings are defined by the user. For instance, the number of iterations, interrogation window size and deformation- and subpixel methods. First PIV attempts performed in this study used conventional settings based on previous studies utilizing echo PIV in humans. [10, 83] Furthermore, the threshold and strength of outlier detection and smoothing parameters influences PIV results. Overly smoothed data generally exhibits a decreased range over which velocities are detected. Especially at locations with high velocities or disturbed flow patterns, smoothing should be used with caution.
Exploring these possible improvements and simply analyzing more data will reveal to what extent the acquired measurements, for instance with lower CBR or shadows, are still good enough for accurate PIV analysis to be performed.

Practical aspects

Beside all technical factors, practical aspects of echo PIV measurements should be considered as well when assessing feasibility. Echo PIV measurements were preformed within one hour with a group of two technical physicians and two vascular technologists. This could be downsized to a one technical physician and one vascular technologist. Navigating to the right locations turned out to be complicated due to the decreased image quality of the images acquired with the three-angled plane wave sequence of the research US machine and the lack of color Doppler. In some cases the microbubbles were used to navigate to a subsequent location and to establish the most optimal view. However, UCA was not always clearly visible. This can be explained in light of the results shown in the previous chapter. Motion of tissue is most likely to be more present in data acquired from patients, hence influencing bubble visualization. The improvements mentioned in Chapter 3 should be explored to enhance bubble visualization, as it is an important feature in data acquisition. Furthermore, the PFA was difficult to visualize in most patients. This was reflected in the first two steps of feasibility assessment.

Future perspectives

An obvious and essential next step would be the addition of streamlines to the obtained vector fields. With the current vector fields it is hard to evaluate if echo PIV can visualize specific blood flow patterns, such as recirculations. This is crucial because the ability to quantify specific blood flow patterns would be an important step in blood flow assessment.

When feasibility of echo PIV is proven, further development in terms of ease-of-use and real-time data visualization is needed in order for it to be clinically practicable. Currently, processing of the echo PIV data is very time-consuming. Accurate calculations of flow derived parameters, for instance a *vector complexity* value, oscillatory shear index or WSS, remain another challenge. [11, 89] Clinical trials in a larger cohort should be performed with follow-up in order to obtain the predictive value of these flow parameters.

4.5 Conclusion

First results of echo PIV near the femoral bifurcation and in the stented SFA are promising. Accurate velocity tracking has been established in two out of five measured locations. More data should be analyzed and improvements in data acquisition, pre-processing and PIV analysis should be explored in order to be able to draw a thorough conclusion regarding feasibility of the technique.

5 Conclusions

An exploratory study in patients has been performed to investigate clinical feasibility of echo PIV as a technique to quantify local blood flow in the femoral bifurcation and stented SFA. Analysis of the first data showed promising results. Accurate blood flow velocity tracking was established in two out of five locations in in the first PIV analyzed patient. Adequacy of PIV analysis seemed to be influenced by the quality of the acquired data in terms of vessel visibility and CBR. Several improvements are suggested and should be explored to optimize data acquisition and PIV analysis.
Based on unexpected observations made during the first clinical echo PIV measurement, in vitro experiments were carried out. Results of the in vitro experiments were able to clarify the unexpected pulse inversion outcomes in real-time bubble visualization. Moreover, the experiments yielded numerous possible improvements in optimally utilizing the non-linear behavior of the microbubbles, which may have direct implications for future studies using echo PIV in patients.

References

[1] Hart- en vaatziekten in nederland 2015: cijfers over heden, verleden en toekomst. https://www.hartstichting.nl/getmedia/b9b5f9df-d00e-44da-bcdd-053d1c18dc07/cijferboek-hartstichting-hart-vaatziekten-nederland-2015.pdf. Accessed: 2019-03-30.

[2] Iftikhar J Kullo and Thom W Rooke. Peripheral artery disease. *New England Journal of Medicine*, 374(9):861–871, 2016.

[3] Mark R Nehler, Mary M McDermott, Diane Treat-Jacobson, Ian Chetter, and Judith G Regensteiner. Functional outcomes and quality of life in peripheral arterial disease: current status. *Vascular Medicine*, 8(2):115–126, 2003.

[4] Gillian C Leng, Amanda J Lee, F Gerald R Fowkers, Maratha Whiteman, Janet Dunbar, Edward Housley, and C Vaughan Ruckley. Incidence, natural history and cardiovascular events in symptomatic and asymptomatic peripheral arterial disease in the general population. *International journal of epidemiology*, 25(6):1172–1181, 1996.

[5] Arif Yurdagul, Alexandra C Finney, Matthew D Woolard, and A Wayne Orr. The arterial microenvironment: the where and why of atherosclerosis. *Biochemical Journal*, 473(10):1281–1295, 2016.

[6] Jeng-Jiann Chiu and Shu Chien. Effects of disturbed flow on vascular endothelium: pathophysiological basis and clinical perspectives. *Physiological reviews*, 91(1):327–387, 2011.

[7] Michael R Jaff, Christopher J White, William R Hiatt, Gerry R Fowkes, John Dormandy, Mahmood Razavi, Jim Reekers, and Lars Norgren. An update on methods for revascularization and expansion of the tasc lesion classification to include below-the-knee arteries: a supplement to the inter-society consensus for the management of peripheral arterial disease (tasc ii). *Annals of vascular diseases*, 8(4):343–357, 2015.

[8] Wai-ki Yiu and Michael S Conte. Primary stenting in femoropopliteal occlusive disease–what is the appropriate role?–. *Circulation Journal*, 79(4):704–711, 2015.

[9] Louai Razzouk, Saurabh Aggarwal, Farzan Gorgani, and Anvar Babaev. In-stent restenosis in the superficial femoral artery. *Annals of vascular surgery*, 27(4):510–524, 2013.

[10] Stefan Engelhard, Jason Voorneveld, Hendrik J Vos, Jos JM Westenberg, Frank JH Gijsen, Pavel Taimr, Michel Versluis, Nico de Jong, Johan G Bosch, Michel MPJ Reijnen, and Erik Groot Jebbink. High-frame-rate contrast-enhanced us particle image velocimetry in the abdominal aorta: First human results. *Radiology*, 2018.

[11] Phillip E Gates, Arati Gurung, Luciano Mazzaro, Kuni Aizawa, Salim Elyas, William D Strain, Angela C Shore, and Robin Shandas. Measurement of wall shear stress exerted by flowing blood in the human carotid artery: Ultrasound doppler

velocimetry and echo particle image velocimetry. *Ultrasound in medicine & biology*, 44(7):1392–1401, 2018.

[12] Michael H Criqui and Victor Aboyans. Epidemiology of peripheral artery disease. *Circulation research*, 116(9):1509–1526, 2015.

[13] Christos Kasapis and Hitinder S Gurm. Current approach to the diagnosis and treatment of femoral-popliteal arterial disease. a systematic review. *Current cardiology reviews*, 5(4):296–311, 2009.

[14] Thomas Zeller. Current state of endovascular treatment of femoro-popliteal artery disease. *Vascular Medicine*, 12(3):223–234, 2007.

[15] Peter Libby, Paul M Ridker, and Göran K Hansson. Progress and challenges in translating the biology of atherosclerosis. *Nature*, 473(7347):317, 2011.

[16] Kenneth Ouriel. Peripheral arterial disease. *The lancet*, 358(9289):1257–1264, 2001.

[17] Ira Tabas, Guillermo García-Cardeña, and Gary K Owens. Recent insights into the cellular biology of atherosclerosis. *J cell Biol*, 209(1):13–22, 2015.

[18] David M Wootton and David N Ku. Fluid mechanics of vascular systems, diseases, and thrombosis. *Annual review of biomedical engineering*, 1(1):299–329, 1999.

[19] Akram M Shaaban and André J Duerinckx. Wall shear stress and early atherosclerosis: a review. *American Journal of Roentgenology*, 174(6):1657–1665, 2000.

[20] James N Topper and Michael A Gimbrone Jr. Blood flow and vascular gene expression: fluid shear stress as a modulator of endothelial phenotype. *Molecular medicine today*, 5(1):40–46, 1999.

[21] Daniel E Conway, Marcie R Williams, Suzanne G Eskin, and Larry V McIntire. Endothelial cell responses to atheroprone flow are driven by two separate flow components: low time-average shear stress and fluid flow reversal. *American Journal of Physiology-Heart and Circulatory Physiology*, 298(2):H367–H374, 2009.

[22] Alexander J Hills, Joseph Shalhoub, Amanda C Shepherd, and Alun H Davies. Peripheral arterial disease. *British Journal of Hospital Medicine*, 70(10):560–565, 2009.

[23] Paul W Wennberg. Approach to the patient with peripheral arterial disease. *Circulation*, 128(20):2241–2250, 2013.

[24] Victor Aboyans, Jean-Baptiste Ricco, Marie-Louise EL Bartelink, Martin Björck, Marianne Brodmann, Tina Cohnert, Jean-Philippe Collet, Martin Czerny, Marco De Carlo, Sebastian Debus, et al. 2017 esc guidelines on the diagnosis and treatment of peripheral arterial diseases, in collaboration with the european society for vascular surgery (esvs) document covering atherosclerotic disease of extracranial carotid and vertebral, mesenteric, renal, upper and lower extremity arteries endorsed by: the european stroke organization (eso) the task force for the diagnosis and treatment of peripheral arterial diseases of the european society of cardiology (esc) and of the european society for vascular surgery (esvs). *European heart journal*, 39(9):763–816, 2017.

[25] Matthew K. Walsworth, Rob M. A. de Bie, Stephen F. Figoni, and Jessica B O'connell. Peripheral artery disease: What you need to know. *The Journal of orthopaedic and sports physical therapy*, 47(12):957–964, 2017.

[26] Jennifer F Wilson. Peripheral arterial disease. *Annals of internal medicine*, 146(5):ITC3–1, 2007.

[27] Stephen B Coffi, Dirk Th Ubbink, Ineke Zwiers, A Johan M van Gurp, and Dink A Legemate. The value of the peak systolic velocity ratio in the assessment of the haemodynamic significance of subcritical iliac artery stenoses. *European Journal of Vascular and Endovascular Surgery*, 22(5):424–428, 2001.

[28] Massimo F Piepoli, Arno W Hoes, Stefan Agewall, Christian Albus, Carlos Brotons, Alberico L Catapano, Marie-Therese Cooney, Ugo Corra, Bernard Cosyns, Christi Deaton, et al. 2016 european guidelines on cardiovascular disease prevention in clinical practice: The sixth joint task force of the european society of cardiology and other societies on cardiovascular disease prevention in clinical practice (constituted by representatives of 10 societies and by invited experts) developed with the special contribution of the european association for cardiovascular prevention & rehabilitation (eacpr). *European heart journal*, 37(29):2315–2381, 2016.

[29] Timothy P Murphy, Donald E Cutlip, Judith G Regensteiner, Emile R Mohler, David J Cohen, Matthew R Reynolds, Joseph M Massaro, Beth A Lewis, Joselyn Cerezo, Niki C Oldenburg, et al. Supervised exercise versus primary stenting for claudication resulting from aortoiliac peripheral artery disease: six-month outcomes from the claudication: exercise versus endoluminal revascularization (clever) study. *Circulation*, 125(2):99–111, 2012.

[30] William A Marston, Stephen W Davies, Brian Armstrong, Mark A Farber, Robert C Mendes, Joseph J Fulton, and Blair A Keagy. Natural history of limbs with arterial insufficiency and chronic ulceration treated without revascularization. *Journal of vascular surgery*, 44(1):108–114, 2006.

[31] Yann Gouëffic, Nellie Della Schiava, Fabien Thaveau, Eugenio Rosset, Jean-Pierre Favre, Lucie Salomon du Mont, Jean-Marc Alsac, Réda Hassen-Khodja, Thierry Reix, Eric Allaire, et al. Stenting or surgery for de novo common femoral artery stenosis. *JACC: Cardiovascular Interventions*, 10(13):1344–1354, 2017.

[32] Gordon Wong, Saba Lahsaei, Joe Aoun, and Lawrence A Garcia. Management of common femoral artery occlusive disease: A review of endovascular treatment strategies and outcomes. *Catheterization and Cardiovascular Interventions*, 93(3):514–521, 2019.

[33] Patrice L Anderson, Annetine Gelijns, Alan Moskowitz, Ray Arons, Lopa Gupta, Alan Weinberg, Peter L Faries, Roman Nowygrod, and K Craig Kent. Understanding trends in inpatient surgical volume: vascular interventions, 1980-2000. *Journal of vascular surgery*, 39(6):1200–1208, 2004.

[34] Vincent L Rowe, William Lee, Fred A Weaver, and David Etzioni. Patterns of treatment for peripheral arterial disease in the united states: 1996-2005. *Journal of Vascular Surgery*, 49(4):910–917, 2009.

[35] George A Antoniou, Nicholas Chalmers, George S Georgiadis, Miltos K Lazarides, Stavros A Antoniou, Ferdinand Serracino-Inglott, J Vincent Smyth, and David Murray. A meta-analysis of endovascular versus surgical reconstruction of femoropopliteal arterial disease. *Journal of vascular surgery*, 57(1):242–253, 2013.

[36] Lars Norgren, William R Hiatt, John A Dormandy, Mark R Nehler, Kenneth A Harris, and F Gerry R Fowkes. Inter-society consensus for the management of peripheral arterial disease (tasc ii). *Journal of vascular surgery*, 45(1):S5–S67, 2007.

[37] Patrick B Metzger, Marilia G Volpato, Maria C Folino, Fabio H Rossi, Ana CG Petisco,

Mohamed H Saleh, Nilo M Izukawa, and Antonio M Kambara. Outcomes after implantation of superflexible nitinol stents in the superficial femoral artery. *Revista Brasileira de Cardiologia Invasiva (English Edition)*, 23(3):220–225, 2015.

[38] Konstantinos Marmagkiolis, Abdul Hakeem, Nishit Choksi, Malek Al-Hawwas, Mohan Mallikarjuna Rao Edupuganti, Massoud A Leesar, and Mehmet Cilingiroglu. 12-month primary patency rates of contemporary endovascular device therapy for femoro-popliteal occlusive disease in 6,024 patients: Beyond balloon angioplasty. *Catheterization and Cardiovascular Interventions*, 84(4):555–564, 2014.

[39] Stephan H Duda, Marc Bosiers, Johannes Lammer, Dierk Scheinert, Thomas Zeller, Vincent Oliva, Alexander Tielbeek, John Anderson, Benjamin Wiesinger, Gunnar Tepe, et al. Drug-eluting and bare nitinol stents for the treatment of atherosclerotic lesions in the superficial femoral artery: long-term results from the sirocco trial. *Journal of Endovascular Therapy*, 13(6):701–710, 2006.

[40] Žana Kavaliauskienė, Rimantas Benetis, Donatas Inčiūra, Nerijus Aleksynas, Rytis Kaupas, and Aleksandras Antuševas. Factors affecting primary patency of stenting for transatlantic inter-society (tasc ii) type b, c, and d iliac occlusive disease. *Medicina*, 50(5):287–294, 2014.

[41] Karen McQuade, Dennis Gable, Greg Pearl, Brian Theune, and Steve Black. Four-year randomized prospective comparison of percutaneous eptfe/nitinol self-expanding stent graft versus prosthetic femoral-popliteal bypass in the treatment of superficial femoral artery occlusive disease. *Journal of vascular surgery*, 52(3):584–591, 2010.

[42] Michel MPJ Reijnen, Laurens A van Walraven, Wilbert M Fritschy, Mare MA Lensvelt, Clark J Zeebregts, M Suzanna Lemson, Otmar RM Wikkeling, Luuk Smeets, and Suzanne Holewijn. 1-year results of a multicenter randomized controlled trial comparing heparin-bonded endoluminal to femoropopliteal bypass. *JACC: Cardiovascular Interventions*, 10(22):2320–2331, 2017.

[43] Hyoung-Bum Kim, Jean Hertzberg, Craig Lanning, and Robin Shandas. Noninvasive measurement of steady and pulsating velocity profiles and shear rates in arteries using echo piv: in vitro validation studies. *Annals of biomedical engineering*, 32(8):1067–1076, 2004.

[44] Lingli Liu, Hairong Zheng, Logan Williams, Fuxing Zhang, Rui Wang, Jean Hertzberg, and Robin Shandas. Development of a custom-designed echo particle image velocimetry system for multi-component hemodynamic measurements: system characterization and initial experimental results. *Physics in Medicine & Biology*, 53(5):1397, 2008.

[45] Sarah Dort, Stephan Muth, Abigail Swillens, Patrick Segers, Guy Cloutier, and Damien Garcia. Vector flow mapping using plane wave ultrasound imaging. In *Ultrasonics Symposium (IUS), 2012 IEEE International*. IEEE, 2012.

[46] Ragnhild Øvland. Coherent plane-wave compounding in medical ultrasound imaging: Quality investigation of 2d b-mode images of stationary and moving objects. Master's thesis, Institutt for fysikk, 2012.

[47] Vincent Chan and Anahi Perlas. Basics of ultrasound imaging. In *Atlas of ultrasound-guided procedures in interventional pain management*, pages 13–19. Springer, 2011.

[48] Maja Cikes, Ling Tong, George R Sutherland, and Jan D'hooge. Ultrafast cardiac

ultrasound imaging: technical principles, applications, and clinical benefits. *JACC: Cardiovascular Imaging*, 7(8):812–823, 2014.

[49] Arati Gurung, Phillip E Gates, Luciano Mazzaro, Jonathan Fulford, Fuxing Zhang, Alex J Barker, Jean Hertzberg, Kunihiko Aizawa, William D Strain, Salim Elyas, et al. Echo particle image velocimetry for estimation of carotid artery wall shear stress: Repeatability, reproducibility and comparison with phase-contrast magnetic resonance imaging. *Ultrasound in medicine & biology*, 43(8):1618–1627, 2017.

[50] Chee Hau Leow, Eleni Bazigou, Robert J Eckersley, CH Alfred, Peter D Weinberg, and Meng-Xing Tang. Flow velocity mapping using contrast enhanced high-frame-rate plane wave ultrasound and image tracking: methods and initial in vitro and in vivo evaluation. *Ultrasound in medicine & biology*, 41(11):2913–2925, 2015.

[51] Hyoung-Bum Kim, Jean R Hertzberg, and Robin Shandas. Development and validation of echo piv. *Experiments in fluids*, 36(3):455–462, 2004.

[52] William Thielicke and Eize Stamhuis. Pivlab–towards user-friendly, affordable and accurate digital particle image velocimetry in matlab. *Journal of Open Research Software*, 2(1), 2014.

[53] John Westerdale, Marek Belohlavek, Eileen M McMahon, Panupong Jiamsripong, Jeffrey J Heys, and Michele Milano. Flow velocity vector fields by ultrasound particle imaging velocimetry: in vitro comparison with optical flow velocimetry. *Journal of Ultrasound in Medicine*, 30(2):187–195, 2011.

[54] Fuxing Zhang, Craig Lanning, Luciano Mazzaro, Alex J Barker, Phillip E Gates, W David Strain, Jonathan Fulford, Oliver E Gosling, Angela C Shore, Nick G Bellenger, et al. In vitro and preliminary in vivo validation of echo particle image velocimetry in carotid vascular imaging. *Ultrasound in medicine & biology*, 37(3):450–464, 2011.

[55] Christian Poelma. Ultrasound imaging velocimetry: a review. *Experiments in Fluids*, 58(1):3, 2017.

[56] Christian Poelma, RME Van der Mijle, Jean-Martial Mari, Meng-Xing Tang, Peter D Weinberg, and Jerry Westerweel. Ultrasound imaging velocimetry: Toward reliable wall shear stress measurements. *European Journal of Mechanics-B/Fluids*, 35:70–75, 2012.

[57] Jesper Udesen, Fredrik Gran, Kristoffer Lindskov Hansen, Jørgen Arendt Jensen, Carsten Thomsen, and Michael Bachmann Nielsen. High frame-rate blood vector velocity imaging using plane waves: Simulations and preliminary experiments. *IEEE transactions on ultrasonics, ferroelectrics, and frequency control*, 55(8):1729–1743, 2008.

[58] Mickael Tanter and Mathias Fink. Ultrafast imaging in biomedical ultrasound. *IEEE transactions on ultrasonics, ferroelectrics, and frequency control*, 61(1):102–119, 2014.

[59] Peter N Burns and Stephanie R Wilson. Microbubble contrast for radiological imaging: 1. principles. *Ultrasound quarterly*, 22(1):5–13, 2006.

[60] Emilio Quaia. *Contrast media in ultrasonography*. Springer, 2005.

[61] Nico de Jong, Ayache Bouakaz, and Folkert J Ten Cate. Contrast harmonic imaging. *Ultrasonics*, 40(1-8):567–573, 2002.

[62] Olivier Couture, Mathias Fink, and Mickael Tanter. Ultrasound contrast plane wave imaging. *IEEE transactions on ultrasonics, ferroelectrics, and frequency control*,

59(12):2676–2683, 2012.

[63] David Hope Simpson and Peter N Burns. Pulse inversion doppler: a new method for detecting nonlinear echoes from microbubble contrast agents. In *Ultrasonics Symposium, 1997. Proceedings., 1997 IEEE*, volume 2, pages 1597–1600. IEEE, 1997.

[64] Harald Becher and Peter N Burns. *Handbook of contrast echocardiography: Left ventricular function and myocardial perfusion*. Springer Science & Business Media, 2012.

[65] Stephanie R Wilson and Peter N Burns. Microbubble-enhanced us in body imaging: what role? *Radiology*, 257(1):24–39, 2010.

[66] Peter N Burns, Stephanie R Wilson, and David H Simpson. Pulse inversion imaging of liver blood flow: improved method for characterizing focal masses with microbubble contrast. *Investigative radiology*, 35(1):58, 2000.

[67] Michalakis Averkiou, Jeff Powers, Dan Skyba, Matthew Bruce, and Seth Jensen. Ultrasound contrast imaging research. *Ultrasound quarterly*, 19(1):27–37, 2003.

[68] Peter JA Frinking, Ayache Bouakaz, Johan Kirkhorn, Folkert J Ten Cate, and Nico De Jong. Ultrasound contrast imaging: current and new potential methods. *Ultrasound in medicine & biology*, 26(6):965–975, 2000.

[69] Qingyu Ma, Yong Ma, Xiufen Gong, and Dong Zhang. Improvement of tissue harmonic imaging using the pulse-inversion technique. *Ultrasound in medicine & biology*, 31(7):889–894, 2005.

[70] Johan Kirkhorn, Sigmund Frigstad, and Hans Torp. Comparison of pulse inversion and second harmonic for ultrasound contrast imaging. In *2000 IEEE Ultrasonics Symposium. Proceedings. An International Symposium (Cat. No. 00CH37121)*, volume 2, pages 1897–1901. IEEE, 2000.

[71] Meng-Xing Tang, Naohisa Kamiyama, and Robert J Eckersley. Effects of nonlinear propagation in ultrasound contrast agent imaging. *Ultrasound in medicine & biology*, 36(3):459–466, 2010.

[72] Jacopo Viti, Hendrik J Vos, Nico de Jong, Francesco Guidi, and Piero Tortoli. Detection of contrast agents: Plane wave versus focused transmission. *IEEE transactions on ultrasonics, ferroelectrics, and frequency control*, 63(2):203–211, 2016.

[73] K Zell, JI Sperl, MW Vogel, R Niessner, and C Haisch. Acoustical properties of selected tissue phantom materials for ultrasound imaging. *Physics in Medicine & Biology*, 52(20):N475, 2007.

[74] Hendrik J Vos, Marcia Emmer, and Nico De Jong. Oscillation of single microbubbles at room versus body temperature. In *2008 IEEE Ultrasonics Symposium*, pages 982–984. IEEE, 2008.

[75] Helen Mulvana, Eleanor Stride, Jo V Hajnal, and Robert J Eckersley. Temperature dependent behavior of ultrasound contrast agents. *Ultrasound in medicine & biology*, 36(6):925–934, 2010.

[76] John Bartlett Segur and Helen E Oberstar. Viscosity of glycerol and its aqueous solutions. *Industrial & Engineering Chemistry*, 43(9):2117–2120, 1951.

[77] Verasonics transducer specifications. `http://verasonics.com/wp-content/uploads/2015/09/Verasonics-transducer_specifications_sheet_Sept2015.pdf`. Accessed: 2018-09-30.

[78] Marije S van der Vee. Feasibility of echopiv in the stented femoral artery. Master's

thesis, University of Twente, 2018.

[79] Che-Chou Shen and Pai-Chi Li. Motion artifacts of pulse inversion-based tissue harmonic imaging. *IEEE transactions on ultrasonics, ferroelectrics, and frequency control*, 49(9):1203–1211, 2002.

[80] Che-Chou Shen, Yi-Hong Chou, and Pai-Chi Li. Pulse inversion techniques in ultrasonic nonlinear imaging. *Journal of Medical Ultrasound*, 13(1):3–17, 2005.

[81] Narendra D Londhe and Jasjit S Suri. Superharmonic imaging for medical ultrasound: a review. *Journal of medical systems*, 40(12):279, 2016.

[82] Ayache Bouakaz, Sigmund Frigstad, Folkert J Ten Cate, and Nico de Jong. Super harmonic imaging: a new imaging technique for improved contrast detection. *Ultrasound in medicine & biology*, 28(1):59–68, 2002.

[83] Jason Voorneveld, Stefan Engelhard, Hendrik J Vos, Michel MPJ Reijnen, Frank Gijsen, Michel Versluis, Erik Groot Jebbink, Nico de Jong, and Johan G Bosch. High-frame-rate contrast-enhanced ultrasound for velocimetry in the human abdominal aorta. *IEEE transactions on ultrasonics, ferroelectrics, and frequency control*, 65(12):2245–2254, 2018.

[84] Denis R Morel, Ian Schwieger, Laurent Hohn, Jacques Terrettaz, Jean B Llull, Yves A Cornioley, and Michel Schneider. Human pharmacokinetics and safety evaluation of sonovue™, a new contrast agent for ultrasound imaging. *Investigative radiology*, 35(1):80, 2000.

[85] Charlie Demené, Thomas Deffieux, Mathieu Pernot, Bruno-Félix Osmanski, Valérie Biran, Jean-Luc Gennisson, Lim-Anna Sieu, Antoine Bergel, Stephanie Franqui, Jean-Michel Correas, et al. Spatiotemporal clutter filtering of ultrafast ultrasound data highly increases doppler and fultrasound sensitivity. *IEEE transactions on medical imaging*, 34(11):2271–2285, 2015.

[86] Jérôme Baranger, Bastien Arnal, Fabienne Perren, Olivier Baud, Mickael Tanter, and Charlie Demené. Adaptive spatiotemporal svd clutter filtering for ultrafast doppler imaging using similarity of spatial singular vectors. *IEEE transactions on medical imaging*, 37(7):1574–1586, 2018.

[87] Jerry Westerweel and Fulvio Scarano. Universal outlier detection for piv data. *Experiments in fluids*, 39(6):1096–1100, 2005.

[88] Uri Shavit, Ryan J Lowe, and Jonah V Steinbuck. Intensity capping: a simple method to improve cross-correlation piv results. *Experiments in Fluids*, 42(2):225–240, 2007.

[89] Anne ECM Saris, Hendrik HG Hansen, Stein Fekkes, Jan Menssen, Maartje M Nillesen, and Chris L de Korte. In vivo blood velocity vector imaging using adaptive velocity compounding in the carotid artery bifurcation. *Ultrasound in medicine & biology*, 45(7):1691–1707, 2019.